



# UQ state-dependent framework for seismic fragility assessment of industrial components

Chiara Nardin <sup>a,b</sup> \*, Stefano Marelli <sup>b</sup> , Oreste S. Bursi <sup>a</sup> , Bruno Sudret <sup>b</sup> ,  
Marco Broccardo <sup>a</sup> ,\*

<sup>a</sup> Department of Civil, Environmental and Mechanical Engineering, University of Trento, Via Mesiano 77, 38123 Trento, Italy

<sup>b</sup> Chair of Risk, Safety and Uncertainty Quantification, Institute of Structural Engineering, ETH Zürich, Stefano-Francini-Platz 5, CH 8093, Zürich, Switzerland

## ARTICLE INFO

### Keywords:

State-dependent fragility functions  
Surrogate modelling  
Polynomial chaos expansion  
Industrial components  
Uncertainty quantification  
Seismic vulnerability

## ABSTRACT

Recently, there has been increased interest in assessing the seismic fragility of industrial plants and process equipment. This is reflected in the growing number of studies, community-funded research projects and experimental campaigns on the matter. Nonetheless, the complexity of the problem and its inherent modelling, coupled with a general scarcity of available data on process equipment, has limited the development of risk assessment methods. In fact, these limitations have led to the creation of simplified and quick-to-run models. In this context, we propose an innovative framework for developing state-dependent fragility functions. This new methodology combines limited data with the power of metamodelling and statistical techniques, namely polynomial chaos expansions (PCE) and bootstrapping. Therefore, we validated the framework on a simplified and computationally efficient MDof system endowed with Bouc-Wen hysteresis. Then, we tested it on a real nonstructural industrial process component. Specifically, we applied the state-dependent fragility framework to a critical vertical tank of a multicomponent full-scale 3D steel braced frame (BF). The seismic performance of the BF endowed with process components was captured by means of shake table campaign within the European SPIF project. Finally, we derived state-dependent fragility functions based on the combination of PCE and bootstrap at a greatly reduced computational cost.

## 1. Introduction

### 1.1. Background and motivation

Assessing structural and non-structural component vulnerability to earthquakes is a key step in modern probabilistic seismic risk assessment [1]. The PEER performance-based earthquake engineering framework has gained significant momentum in this field, thanks to its inherently versatile formulation. Its strength lies in a simple yet effective implementation of the total probability theorem, which allows one to decouple and then combine the output of probabilistic seismic hazard analysis with fragility, damage, and loss analysis. To this end, the fragility analysis step offers the critical link between seismic hazard and structural modelling, since it estimates conditional probability of attaining or exceeding a specified damage state (DS), given an intensity measure (IM) of earthquake motion.

Initially introduced for nuclear safety evaluation, fragility curves are nowadays widely used, ranging from assessment of collapse risk to loss estimation, from resilience quantification at individual scale to community scale [2–4], etc.

In recent years, several novel methodological contributions to fragility analysis have been made. They include the development of multivariate fragility functions [5], the introduction of seismic fragility analysis based on a combination of real [6] and artificial ground motions and surrogate modelling [7], and the consideration of both state [8] and time-dependent fragility [9,10]. Nonetheless, the majority of the past research focus was committed to characterize the damage transition from a pristine state, i.e., no seismic damage, to a more severe damage state for structures subjected to a single ground motion. Conversely, significantly less research has been devoted to state-dependent fragility modelling, which (i) can capture the damage accumulation due to sequential seismic events, and (ii) enables fragility estimations of structures with different initial damage states. To the best of our knowledge, only the first attempt has been made by [8,11], [12], and [13].

As a matter of fact, the compounding effect of damage accumulation and disruption caused by sequences of earthquakes (such as in Wenchuan (2008), Tohoku (2011) and central Italy (2016)), has highlighted the importance of accurately capturing the effect of irreversible

\* Corresponding authors.

E-mail addresses: [chiara.nardin@unitn.it](mailto:chiara.nardin@unitn.it), [cocardin@ethz.ch](mailto:cocardin@ethz.ch) (C. Nardin), [marco.broccardo@unitn.it](mailto:marco.broccardo@unitn.it) (M. Broccardo).

## Glossary and Nomenclature

<b>BF</b>	Braced Frame
<b>DBE</b>	Design Basis Earthquake
<b>DS</b>	Damage State
<b>EDP</b>	Engineering Demand Param.
<b>FE</b>	Finite Element
<b>GMM</b>	Ground Motion Model
<b>gms</b>	ground motions
<b>IM</b>	Intensity Measure
<b>MCS</b>	Monte Carlo Simulation
<b>NLTHA</b>	Non-Linear Time History An.
<b>NSC</b>	Non-Structural Components
<b>PC</b>	Principal Component
<b>PCA</b>	Principal Component An.
<b>PCE</b>	Polynomial Chaos Expansions
<b>PSHA</b>	Probabilistic Seismic Hazard An.
<b>SSE</b>	Safe Shutdown Earthquake
<b>QoI</b>	Quantity of Interest
<b>UQ</b>	Uncertainty Quantification
$\gamma; \hat{\gamma}$	True/surrogate QoIs
$\mathcal{M}_{FE}(\cdot)$	FE model
$\mathcal{M}_{PCE}(\cdot)$	PCE model
$A(t, \mathcal{X})$	GMM seis. sequence
<b>IM; <math>\widehat{IM}</math></b>	IMs and pseudo-IMs
$D_s$	Design of Experiment
$\epsilon_{gen}$	Relative generalization error
$\epsilon_{LOO}$	Leave-one-out error
$\epsilon_{emp}$	Empirical error
$\beta_{eff}$	Efficiency criterion
$D_{KL}$	Kullback–Leibler divergence dist.
$D_{KS}$	Kolmogorov–Smirnov dist.

damage accumulation for a reliable risk assessment. In this respect, recent research, see, among others, [14] and [15]), deeply investigated the effects of sequential seismic events and damage accumulation on structural performances.

On one side, procedures for selecting ground motions for sequences of events have been the subject of thorough studies. The authors in [16] recommend using seismic sequences that combine main-shock and after-shock record pairs, because they naturally capture and preserve within-sequence correlations. Such seismic sequence record sets are particularly advantageous given the continuous expansion and refinement of databases containing these records. When additional data is required, ground motion models can be employed to effectively populate the event sequences.

On the other, advances in non-linear structural response simulations have yielded more accurate modelling of complex and multi-mode systems. These developments provide better insights into critical structural issues and the performance of both structures and their non-structural components (NSCs). A more thorough discussion of these issues is reported in [17].

Moreover, significant efforts have been made to further investigate the coupling effects between the main structure and NSCs, both numerically [18,19], and experimentally [20,21]. An important milestone can be found in NIST GCR 17-917-44 [22] that summarizes a year-long study, which collected and documented the body of available knowledge related to the seismic performance of NSCs for civil and industrial structures. Once again, since NSCs for industrial plants account for the majority of direct property losses due to earthquake damage [18], they were identified as a top priority in seismic risk assessment. However,

to limit costly and disruptive non-structural damage is challenging, due to the need of predictive non-linear dynamic analysis for complex systems with strong coupling interactions with NSCs. They are mostly limited by available computational resources. In addition, the computation of fragility analysis requires a large number of non-linear time history analyses (NLTHA), limiting *de facto* the total number of possible simulations.

This issue is central in simulation-based uncertainty quantification (UQ), which is tackled by replacing the computationally expensive NLTHA of finite element (FE) models with an equivalent surrogate model. In fragility assessment, researchers have adopted different metamodeling techniques to reduce the computational burden of extensive simulations. These methods also integrate deterministic models with limited observational data, as demonstrated in [23,24].

Among the catalogue of families of surrogate models, polynomial chaos expansions (PCE) [25], Kriging, firstly in [26] and, more recently, in [27], and neural networks, as in [1,28], have arguably become the most popular in civil engineering, since they provide more than just an approximation to the underlying computational model. In particular, they additionally yield analytical estimates of the response moments of the model, sensitivity indices or confidence levels for their own predictions. For example, [29] estimated the full conditional probability distribution of engineering demand parameter (EDP) conditioned on IMs by means of stochastic PCE. Instead, the authors in [1] proposed a fragility modelling approach based on artificial neural networks for the initial and final damage classification. Moreover, [7] adopted hierarchical Kriging to compute a multi-fidelity surrogate that fuses the predictions of multiple models for fragility assessment. An in-depth literature review of the current state-of-the-art in surrogate modelling for reliability assessment is presented in [30,31]. Undoubtedly, one of the most significant benefits of surrogate models is their computational efficiency after training, allowing for millions of model evaluations per second, even on common end-user hardware. This enables the estimation of empirical fragility functions, as addressed in the literature by the global earthquake model [32,33].

### 1.2. Scope and core contribution

On these premises, this paper presents a novel UQ-based framework for efficiently deriving state-dependent fragility curves of industrial system components. This approach blends data from a reduced number of complex and expensive sequential NLTHAs with cutting-edge metamodeling techniques.

This paper provides the following core contributions:

1. it proposes an innovative framework for developing state-dependent fragility functions, advancing current methodologies in risk assessment;
2. it integrates limited datasets with advanced metamodeling and statistical techniques, specifically PCE and bootstrapping;
3. it showcases validation on simplified models and application to critical, real-world industrial NSCs;
4. it ensures computational efficiency and facilitates seamless integration of experimental data within the developed framework.

In detail, the paper is organized as follows. In Section 2, we present the heuristics and the novel framework for state-dependent fragility assessment. In Section 3, we validate the methodology on an inexpensive-to-evaluate benchmark case study. Specifically, state-dependent fragility functions derived from brute-force Monte Carlo Simulation (MCS) are compared with surrogate-based MCS. In Section 4, we applied the framework to a real industrial case study. Precisely, the case study deals with a critical NSC installed on the steel braced frame (BF) substructure, i.e. a vertical tank, as part of the project SPIF [20]. Finally, we provide in Section 5 a summary of the main findings as well as future development perspectives.



Fig. 1. Transition state (a) matrix and (b) diagram, respectively.

## 2. A state-dependent fragility analysis framework

Limited by the availability of time and information, risk-informed assessments are commonly carried out on the basis of simplified and quick-to-evaluate models. However, as highlighted in the recent NIST GCR 17-917-44 report [22] devoted to industrial facilities, these proven strategies lead to neither economically viable nor rational designs. On these premises, this Section presents the heuristic of a novel framework for system vulnerability assessment. Specifically, based on a combination of experimental data and surrogate models, the proposed methodology enables the computation of state-dependent fragility curves that consider several aspects of the problem.

State-dependent fragility curves are defined as a class of fragility curves conditioned not only by a measure of seismic intensity  $\text{IM}$  (which in generalized form is a vector), but also by the initial state of (discrete) damage  $DS_i$  of the structure (see, [8]). Hence, state-dependent fragilities enable the assessment of the vulnerability of a system that has already experienced damage, as defined by the generalized equation:

$$\begin{aligned} \mathbb{P}[DS_j | DS_i, \text{IM} = im] &= \mathbb{P}[DS \geq DS_j | DS_i, \text{IM} = im] \\ &\quad - \mathbb{P}[DS \geq DS_{j+1} | DS_i, \text{IM} = im], \end{aligned} \quad (1)$$

for  $j > i$ , and  $i$  indices ranging among the identified and most severe damage limit states. Fig. 1(a) shows the generalized transition probability state matrix for a system with three possible levels of damage, i.e.,  $DS_0$  to  $DS_2$ . Each row of the matrix represents the initial damage state or level; whilst each column indicates the final damage state. Each bin represents the transition probability between the initial (row) and final (column) state, including the permanence within the same level. The lower triangular part of the matrix represents the recovery processes of the investigated system, which, for brevity, we do not consider in this paper. Moreover, the ultimate damage limit state  $DS_2$  is considered an absorption state, i.e., a condition that, cannot be exited or recovered once reached. A typical example would be the collapse of the structural system. Similarly, Fig. 1(b) shows the Markovian diagram underlying the transition state matrix, e.g., the allowable jumps between the three-level damage states.

State-dependent fragility analysis requires a vast number of NLTHAs because each position of the transition matrix needs to be sufficiently populated. As a consequence, time histories of multiple seismic events, e.g., seismic sequences, are cast and applied as input for the NLTHAs. This enables us to cover each transition state and different damage initial configurations effectively. Then, the structural and non-structural system performances are clustered according to the damage reference metric. Hence, either empirical or parametric fragility functions are derived, conditioned on the initial damage state condition and the  $\text{IM}$  of the seismic input.

Fig. 2(a) describes the fundamental steps of the workflow, i.e., from the FE and seismic input models definition (steps  $\mathcal{A}$  –  $\mathcal{B}$ ) to the complete NLTHAs and fragility computations (step  $\mathcal{C}$ ). However, when considering realistic computational models, the significant computing demands of an extensive set of sequential NLTHAs generally hinder this

direct derivation of state-dependent fragilities, as in step  $\mathcal{C}$  upper-right corner of Fig. 2(a).

To tackle this limit, the global UQ framework developed in [34,35] is adapted in the proposed methodology. The following three steps are used to define the UQ problem: (i) step  $\mathcal{A}$ , i.e., the definition of the computational model  $\mathcal{M}(\cdot)$ ; (ii) step  $\mathcal{B}$ , description of the input parameters; (iii) step  $\mathcal{C}$ , propagation of the uncertainties and processing of the quantities of interests (QoIs).

Specifically, in the proposed framework, for the steps  $\mathcal{A}$  –  $\mathcal{B}$ , we first perform a given number of sequential NLTHAs:

$$\mathcal{Y} = \mathcal{M}(\mathcal{X}) = \mathcal{M}_{FE} \circ A(t, \mathcal{X}) = \mathcal{M}_{FE}(A(t, \mathcal{X})), \quad (2)$$

where  $A(t, \mathcal{X})$  is a given seismic sequence generated by a stochastic site-based ground motion model (GMM), and  $\circ$  represents the function composition.  $\mathcal{X}$  is a high-dimension random vector which represents both the epistemic (i.e., the stochastic nature of the model parameters), and the aleatory uncertainties (i.e., the Gaussian random variables representing the Gaussian noise). Specifically,  $\mathcal{X} = [\mathcal{X}_1, \dots, \mathcal{X}_j, \dots, \mathcal{X}_M]^T$ , where  $\mathcal{X}_j$  is a random vector which represents the stochastic nature of a given ground motions (gms) and  $M$  the total number of seismic events that constitute the seismic sequence. Moreover,  $\mathcal{M}_{FE}(\cdot)$  represents the computationally intensive FE model;  $\mathcal{Y}$  a random vector that collects the QoIs of the case study. In particular,  $\mathcal{Y} = [\mathcal{Y}_1, \dots, \mathcal{Y}_j, \dots, \mathcal{Y}_M]^T$ , where  $\mathcal{Y}_j$  is the time series response of the associated  $\mathcal{X}_j$  random seismic event.

Next, instead of computationally intensive FE models, cost-effective metamodels for each initial damage level—i.e., rows of the transition matrix of Fig. 1(a)—are tailored on the physics-informed problem and trained on a much smaller dataset. In particular, the QoIs resulting from the NLTHAs are clustered according to the predefined damage initial states, i.e., the number of rows of the transition state matrix of Fig. 1(a). For clarity, only the allowable transition state jumps are sketched. The clustering determines the pairs of  $(x_j, y_j)$ , where  $j$  identifies each gm of the seismic sequences. This step serves to define different designs of experiment depending on the initial state of the structure. Specifically, we identify the different design of experiment with  $D_s$ , where  $s$  identifies the initial state of the structure, i.e.,  $s \in \{DS_0, DS_1\}$ . In the following step, a low-dimensional input representation is used instead of the time series sequences to build a time-invariant surrogate model. Specifically, we used a vector of  $\text{IM}_j$ , following the classical approach of vector-PSHA analysis.

The full list of the considered 41 IMs is collected in Table A.1 of the Appendix A. Since among the list of IM several of them are strongly correlated, we seek specific patterns that allow dimensionality reduction. Therefore, we perform principal component analysis (PCA), to obtain a low dimension vector  $\widehat{\text{IM}}_j$ , which can be interpreted as a vector of uncorrelated pseudo-IMs. Particularly, PCA was used to select the least number of principal components (PCs) to satisfactorily characterize  $\widehat{\text{IM}}_j$ . Finally, we build PCE surrogate models based on the pairs  $(\widehat{\text{im}}_j; y_j)$ :

$$\widehat{\mathcal{Y}} = \mathcal{M}_s^{PCE} (\widehat{\text{IM}}), \quad (3)$$

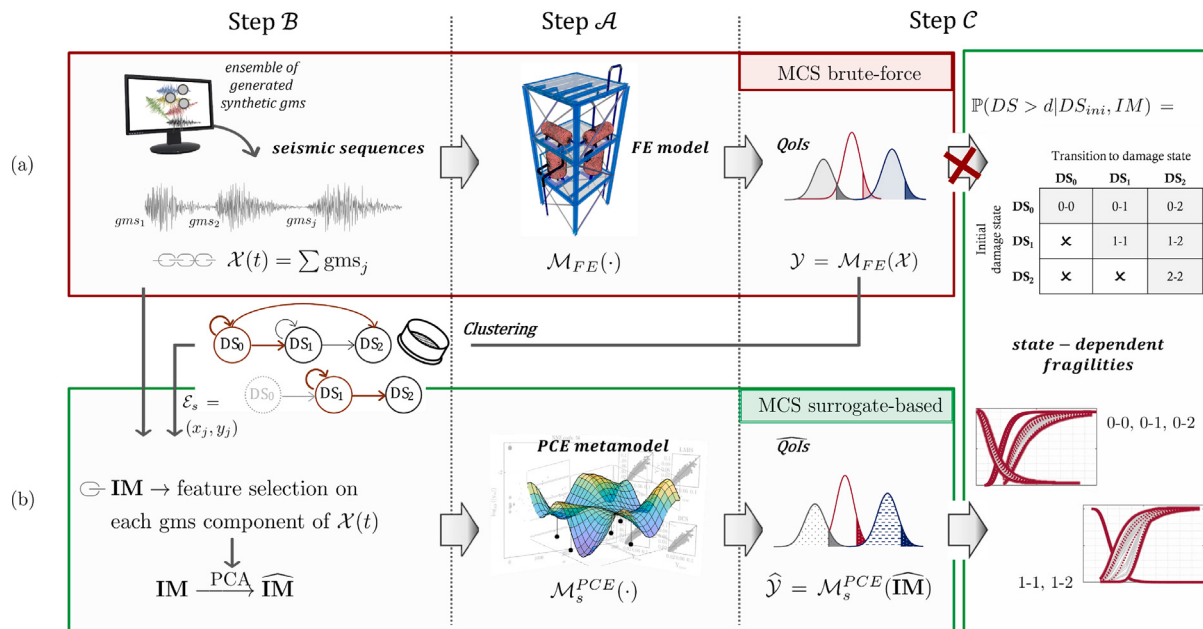


Fig. 2. Step A to C of the (a) brute-force MCS method, and (b) the surrogate-based MCS method for state-dependent fragility assessment.

where  $\mathcal{M}_s^{PCE}(\cdot)$  is the PCE surrogate model;  $\hat{\mathcal{Y}}$  is the vector collecting the surrogated Qols;  $s \in [DS_0; DS_1]$  identifies the initial state of the structure. The vast number of MCS surrogate-based analyses enables us to derive non-parametric state-dependent fragilities functions, as defined in Eq. (1).

Moreover, notice that the framework is not intrusive, meaning that the complex FE model is completely decoupled from the UQ analysis. This allows FE experts to work independently from UQ experts.

In the following Sections, the proposed UQ-based framework is applied twice. In Section 3 on an computationally efficient benchmark case study, to validate the methodology and to illustrate its key steps and tools. Then, in Section 4, we derive state-dependent fragility functions for a vertical tank installed on the industrial mock-up of the SPIF project.

### 3. Benchmark case: Hysteretic MDof system

To test the validity of the proposed framework, we examine the case of an equivalent mechanical computationally efficient multiple-degree-of-freedom (MDof) shear-type system with Bouc–Wen hysteresis. This allows us: (i) to perform a vast number of sequential NLTHAs, and (ii) to evaluate state-dependent fragilities in terms of the inter-storey drift ratio (ID-ratio). Then, the MCS brute-force fragilities are quantitatively and qualitatively compared with the surrogate-based MCS fragilities, derived by applying the UQ-based framework of Section 2.

#### 3.1. Step A—Computational model description

According to the scheme depicted in Fig. 2, the MDof system belongs to step A of the framework, i.e., the definition of the numerical model. The benchmark case study is a 2D condensation of the complex 3D industrial frame, namely SPIF #2 system. Conversely, the full 3D system is studied in Section 4.1.

The SPIF #2 project focused on investigating the seismic behaviour of a prototype multi-storey BF structure equipped with complex secondary industrial components by means of shaking table tests. More details on the project can be found in [17], whilst the shake table test campaign and system performance are described in [20]. The primary objective of the MDof model is to efficiently capture the displacement and shear response time histories at each floor level of the complex BF

system. To allow the execution of a significant number of NLTHAs, a strong emphasis on minimizing the computational resources and time is devoted.

In this context, the engineering demand parameter (EDP) is represented by the maximum ID-ratio. Thus, according to Table C1-3 *Structural Performance Levels and Damage* of FEMA 356 [36], the identified damage metrics DS<sub>i</sub> are 0.5% and 2.0% of the ID-ratio, for Immediate Occupancy (IO) and Collapse Prevention (CP) limit states, respectively. The numerical model implemented in-house with MATLAB® is defined by the system of equations of motion,

$$\mathbf{M} \ddot{\mathbf{u}}(t) + \mathbf{C} \dot{\mathbf{u}}(t) + \mathbf{R} [\mathbf{u}(t), \dot{\mathbf{u}}(t)] = -\mathbf{M} \mathbf{1} \ddot{u}_g(t), \quad (4)$$

where  $\mathbf{M}$  and  $\mathbf{C}$  are calculated from the experimental data collected during the SPIF #2 test campaign [20]–[17];  $\mathbf{R}[\cdot]$  is the non-linear nodal restoring force vector, detailed in Eq. (5);  $\mathbf{1}$  a vector of 1s of size equal to the total DoFs of the system; and  $\ddot{u}_g$  is the stochastic base input, i.e., a realization of the process  $A(t, \mathcal{X})$ , later on presented in Eq. (7) of Section 3.2. Specifically, the Bouc–Wen model was chosen to define the non-linear relation in  $\mathbf{R}[\cdot]$ :

$$\mathbf{R} [u_i(t), \dot{u}_i(t)] = k_{0,i} [\alpha u_i(t) + (1 - \alpha) z_i(t)] \quad (5)$$

where the subscript  $i$  refers to each DoF of the system, ranging from 1 to 3;  $\alpha$  is a parameter that controls the degree of inelasticity,  $k_{0,i}$  is the initial elastic stiffness for each  $i$ -DoF; and  $z_i$  is the hysteretic  $i$ -DoF response governed by the following law:

$$\dot{z} = \frac{D \dot{u} - \{\beta |\dot{u}| z |z|^{n-1} + \gamma |z|^n \dot{u}\} \cdot v}{\eta}. \quad (6)$$

In Eq. (6),  $\{\alpha, \beta, \gamma, D, \delta v, \delta \eta\}$  are model parameters, the values of which are reported in Table 1 along with the structural properties of the system. The comprehensive description of the implemented model is presented in [37]. Fig. 3 compares the hysteresis at the top level for the reduced MDof Bouc–Wen-based model versus the full FE BF model under seismic excitation.

#### 3.2. Step B—Input definition

Sequential chains of seismic events derived from the site-based GMM of [38] are used as the excitation. We consider the far-field GMM scenario described in [20] for the experimental test campaign of SPIF

**Table 1**  
Bouc-Wen parameters for the MDof system.

Parameter	Value
$\alpha, n, \beta_N, \gamma_N$	[–] [0.01; 1.5; 0.167; 0.50]
$\delta D, \delta v, \delta \eta$	[–] [0.002; 1.00; 1.00]E–08
$K_0$	[N/m] [1.72; 1.77; 0.96]E+07
$M$	[kg] [9.5; 14.5; 12.4]E+03

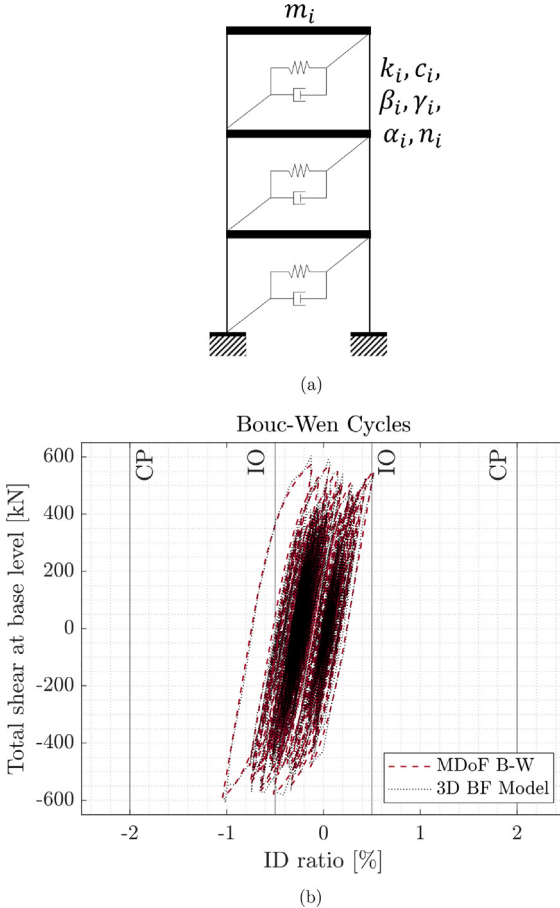


**Fig. 3.** (a) Schematics of the 2D MDof system; (b) comparison of the hysteretic cycles at the top level of the 2D MDof and the 3D BF model.

#2. Briefly, the GMM is based on a modulated and filtered discretized white-noise process described by the following equation:

$$A(t, \mathcal{X}) = q(t, \Theta_q) \left[ \frac{\sqrt{2\pi S \Delta t}}{\sigma_h(t)} \sum_{l=1}^k h[t - t_l, \Theta_h(t_l)] \cdot Z_l \right] \text{ with } t_k \leq t < t_{k+1}, \quad (7)$$

where  $q(t, \Theta_q)$  is the modulating function,  $Z_l$  denote the standard normal Gaussian Random Variables, and  $\sigma_h^2 = 2\pi S \Delta t \sum_{l=1}^k h^2[t - t_l, \Theta_h(t_l)]$  the standard deviation of the discrete filtered white-noise process. Moreover,  $t_l$  is a set of equally spaced time points (with  $l = 0, 1, \dots, L$ ,  $t_0 = 0$ , and  $t_L$  representing the total duration of the motion) and  $k = \text{int}(t_L/\Delta t) = 0, 1, \dots, L$ . As shown in [38],  $\Theta_q = [I_a, t_{mid}, D_{5-95}]$  are the parameters of the modulating function, while  $\Theta_h = [\omega_{mid}, \dot{\omega}, \zeta]$  are the filter parameters. Provided with this representation,  $\mathcal{X}$  (in Eq. (2)) is written as follows  $\mathcal{X} = [I_a, D_{5-95}, t_{mid}, \omega_{mid}, \dot{\omega}_{mid}, \zeta_f, Z_1, \dots, Z_L]$ . Observe that  $\mathcal{X}$  includes both an aleatory component represented by the Gaussian random variables and an epistemic component represented by the randomized GMM parameters.

The marginal distributions of the GMM parameters are summarized in Table 2. In [20], these distributions were inferred from selected INGV and ITACA datasets based on the following assumptions: (i) distance

fault-site  $R > 10[\text{km}]$ ; (ii) moment magnitude  $M_w > 5.5$ ; (iii) main shock seismic events only; (iv) strong motion intensities expressed in terms of  $PGA > 0.075[\text{g}]$ . The complete list of the selected natural records and their characteristics is provided in [20].

Then, the calibrated GMM is used to generate an ensemble of  $10^4$  simulated gms. Based on the following assumptions: (i) mainshock events characterized by long return periods, (ii) no recovery/restoring processes, and (iii) negligible degradation effects with respect to seismic damage, gms are randomly extracted from the generated synthetic gms ensemble to compose sequences of seismic time histories, as sketched in Fig. 2(a)-Step B. Observe that we do not consider after-shock sequences, but only sequences of main shock events.

Next, we construct the dataset in the following way. We simulate  $10^4$  gms and then we randomly generate a sequence of 10 seismic events by randomly permuting the  $10^4$  gms. Thus, the resulting artificial dataset comprises  $10^3$  sequences of 10 gms. Finally, we reproduce 100 of such datasets. In particular, the generation of the GMM parameters is sampled using the 100 predefined seeds (for reproducibility). Notice that the white noise is not reproducible.

The adoption of earthquake sequences allows for considering seismic damage accumulation through time, thus mimicking the effect of non-pristine initial conditions on the structure.

### 3.3. Step C—QoI response

#### 3.3.1. Brute-force MCS for state-dependent fragility functions

A total amount of  $10^6$  sequential NLTHAs were performed, thanks to the minimal computational effort required by a single sequential NLTHA.<sup>1</sup> For each simulation, the initial and final damage configurations were identified based on the EDP. Next, simulations were clustered according to the initial and the final damage state level associated with each ground motion of the seismic sequence, as in Fig. 4. Thus, six combinations among initial-final damage configurations are possible: '0-0', '0-1', '0-2', '1-1', '=1-2', '2-2'. Those represent the transition states of the system, as sketched in Fig. 1(a). Specifically, the '0-0', '0-1', '0-2' identify, given a pristine  $DS_0$  initial state condition, the permanence in the  $DS_0$  and transition to damage state level  $DS_1$  and  $DS_2$ , respectively. Similarly, '1-1', '1-2' identify the permanence in  $DS_1$  and transition to damage state level  $DS_2$ , given an initial damage state level  $DS_1$ . Finally, the '2-2' refers to the absorption state of collapse.

Fig. 5(a) collects the numbers of clustered results of the MCS, while Fig. 5(b) the percentages. Nearly 74% of the total simulations exhibited an initial damage level of  $DS_1$ , with approximately 70% concentrated within the '1-2' cluster. Conversely, around 20% of simulations were performed with no initial damage, e.g.,  $DS_0$ . The remaining 6% of simulations resulted in an absorption collapse state. According to Eq. (1), to evaluate state-dependent fragilities, an optimal IM, or a vector of optimal IMs, needs to be defined.

To do so, we implemented an efficiency criterion,  $\beta_{eff}$ , based on the dispersion of fragility function estimates due to aleatory variability. In other words, for a given IM, this criterion minimizes the dispersion of the conditional distribution of EDP (and consequently the damage estimate) with respect to the aleatory component of the ground motion model. As illustrated in Fig. 6, we define efficiency in terms of the area enclosed between the 90th percentile quantiles of the fragility functions, which serves as a practical measure of dispersion: the smaller the area, i.e., the lower the dispersion, the lower the value of  $\beta_{eff}$ . Thus, the optimal  $\beta_{eff}$  corresponds to the case with the least dispersion. However, since the long list of IMs ranging among different scales, we wanted a normalized criterion. Hence, we decided to consider only three points on each IM scale where to compute the  $\beta_{eff}$  index. Those

<sup>1</sup>  $\approx 3\text{s}$  on an Intel(R) Core(TM) i9-10900K CPU @3.70 GHz, 10 Core(s)—128 GB RAM.

**Table 2**  
Probabilities density distributions of the parameters of the site-based GMM.

Model parameters		Units	Distribution	$\mu$	$\sigma$	Distribution bounds
$I_a$	Arias Intensity	[m/s]	Log-normal	-0.46	0.51	(0; $+\infty$ )
$D_{5-95}$	Time interval of 95% of the $I_a$	[s]	Log-normal	2.21	0.23	(0; $+\infty$ )
$t_{mid}$	Time interval of 45% of the $I_a$	[s]	Log-normal	1.698	0.21	(0; $+\infty$ )
$\omega_{mid}/2\pi$	Filter frequency at $t_{mid}$	[Hz]	Uniform	4.8	1	[3.8; 5.8]
$\zeta_f$	Filter damping ratio	[–]	Uniform	0.35	0.1	[0.25; 0.45]

\* $\dot{\omega}_{mid}$ , rate of change of frequency with  $t$ , is assumed constant and equal to -0.5.

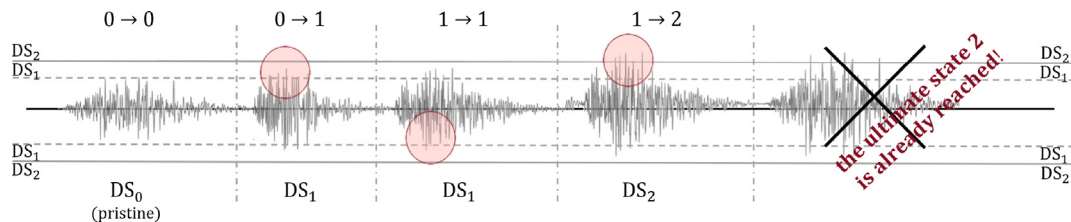


**Fig. 4.** Example of seismic sequence time history response clustered according to the initial and final damage state level, i.e., ranging from DS<sub>0</sub> (pristine) to DS<sub>2</sub> (collapse).

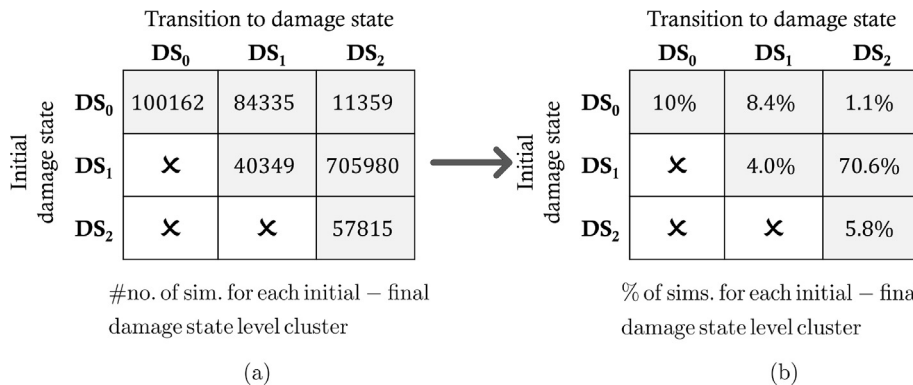


**Fig. 5.** Transition state matrices: (a) counters and (b) percentages of simulation for each initial–final damage state level cluster, respectively.

are indicated with  $x_q$  and represent the 25th – 50th – 75th quantiles of each marginal IM distribution of Table A.1.

Next, to measure the dispersion, we evaluate the 90th inter-quantile range IQR on those  $x_q$  points and sum them for each IM. Finally, the optimal  $\beta_{eff}$  is the minimum among the  $IM_i$ . Eq. (8) describes the criterion:

$$\beta_{eff}(IM_i) = \min \left( \sum_{x_q} IQR_{x_q}(IM_i) \right)^{0.90}, \quad (8)$$

with  $IM_i$  ranging across the 41 elements of the vector **IM** defined in Table A.1. Next the optimal IM is selected as follow  $IM^* = \arg\min_{IM_i} \beta_{eff}(IM_i)$ .

This procedure is applied for each transition state. It follows that transitions can have different optimal  $IM^*$ s. The collection of the optimal transition  $IM^*$ s defines the optimal vector **IM**<sup>\*</sup>, which is used to construct state-dependent fragility functions. It is important to note that this definition differs from the classical notion of efficiency used in fragility analysis (e.g., [39,40], and references therein), where efficiency is generally defined in terms of the homoscedastic variance in a regression analysis on the log scale between **IM** and **EDP**.<sup>2</sup>

At this stage, brute-force MCS on cost-effective systems allows us to reach a full probabilistic description of fragilities. Given the vast

<sup>2</sup> Observe that, without loss of generality, this classical criterion can still be applied to each individual seed simulation to obtain a statistical measure of efficiency.

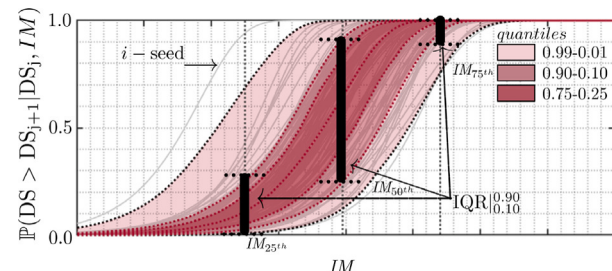


**Fig. 6.**  $\beta_{eff}$  criterion explained: step (i), determine the  $IM_{25th,50th,75th}$  locations on the marginal IM; step (ii), evaluate the  $IQR^{0.90}_{0.10}$  on those locations; step (iii), repeat  $\forall IM_i$  and find the minimum.

number of simulations, empirical fragilities were evaluated for each transition state. Specifically, non-parametric curve-fitting on the cumulative distributions of data against the optimal IM was implemented, as in [32]. Fig. 7 represents the collection of state-dependent fragility functions based on **IM**<sup>\*</sup>. Notice that this Figure does not represent the transition matrix defined in Eq. (1). In fact, this is used to highlight the components of  $\mathbf{IM}^* = [\text{PGA}, I_{RG,a}, \text{ASI}, E-\text{ASA}_{R80}]$ .

Each one of the 100 MCS seeds is associated with a grey line. The curves representing the 90% confidence bounds are displayed in a dashed-dotted dark red style, while those for the 50% confidence bounds are represented with dashed lines. The first row, corresponding to a pristine initial damage state condition, is characterized mainly by

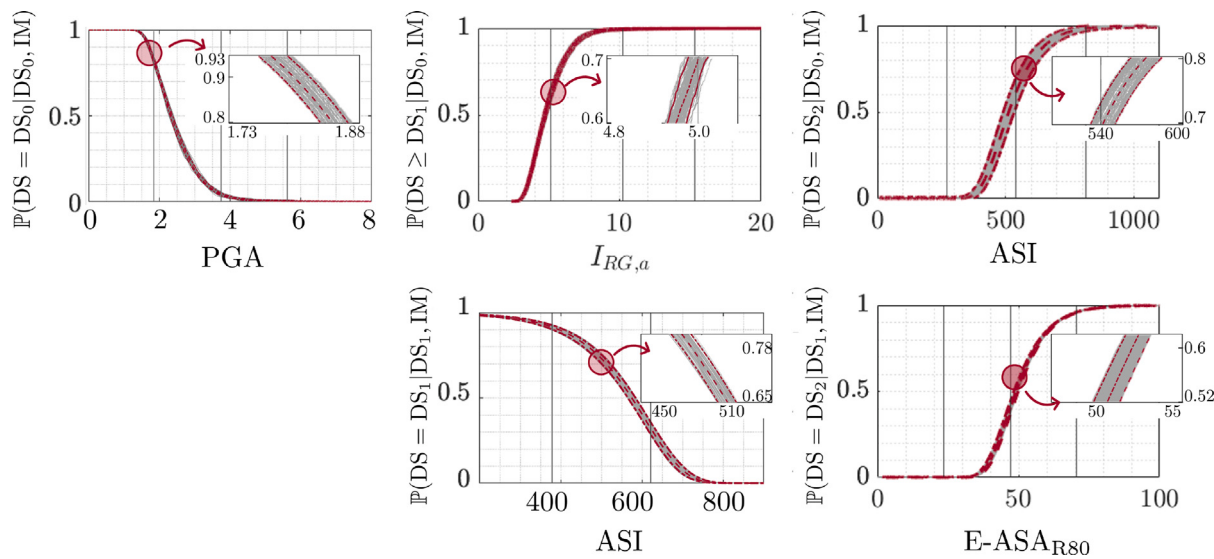


**Fig. 7.** Brute-force MCS state-dependent fragility functions: grey lines represent single seed simulations; dashed-dot dark-red lines depict the 90% confidence bounds, whilst dashed-dark red ones the 50%. Different IMs are adopted in x-axes, according to the optimal  $\beta_{\text{eff}}$  for each transition state.

**Table 3**

Brute-force MCS state-dependent fragility functions: top five  $\beta_{\text{eff}}$  efficiency indices for each transition state.

Frag. '0-0' optimal IM	$\beta_{\text{eff}}$ index	Frag. '0-1' optimal IM	$\beta_{\text{eff}}$ index	Frag. '0-2' optimal IM	$\beta_{\text{eff}}$ index	Frag. '1-1' optimal IM	$\beta_{\text{eff}}$ index	Frag. '1-2' optimal IM	$\beta_{\text{eff}}$ index
PGA	9.60E-02	$I_{RG,a}$	1.83E-02	ASI	8.59E-02	ASI	7.00E-03	E - ASA <sub>R80</sub>	1.96E-02
IC	1.01E-01	PGA	2.10E-02	EPA	9.55E-02	EPA	7.70E-03	E - ASA <sub>R200</sub>	2.24E-02
$I_{RG,a}$	1.03E-01	$I_{RG,v}$	2.50E-02	RMS(ii)	9.82E-02	PGA	7.70E-03	E - ASA <sub>R100</sub>	2.31E-02
E - ASA <sub>R80</sub>	1.07E-01	E - ASA <sub>R80</sub>	2.62E-02	PGA	9.83E-02	$I_{RG,v}$	7.90E-03	E - ASA <sub>R150</sub>	2.63E-02
RMS(ii)	1.10E-01	PGD	2.63E-02	E - ASA <sub>R80</sub>	1.17E-01	$I_{RG,a}$	8.10E-03	I <sub>RG,a</sub>	4.10E-02

PGA-derived IMs, while the second row is characterized by  $S_a$ -related features. Furthermore, it becomes evident that the optimal IM changes as moving toward more severe damage states or starting from a non-pristine initial condition. Particularly, the evolving IM is characterized by features capable of capturing reductions in stiffness due to the accumulation of damage, and shifts in the frequency range of the structure, such as E - ASA<sub>R\*</sub>. The  $\beta_{\text{eff}}$  values are collected in [Table 3](#).

A limitation of this approach is that one needs to develop a fragility model based on  $\text{IM}^*$ , which can become computationally demanding (in terms of memory allocation). In this specific example, the state-dependent fragility models,  $\mathbb{P}(DS_j | DS_i, \text{IM}^*)$  are four-dimensional functions. Moreover, a vector-based seismic risk analysis needs to be developed to use this model directly. While this is not a limit in a Monte-Carlo-based seismic risk analysis, it becomes prohibitive for direct integration. A more straightforward approach is to use state-dependent fragilities as functions of one optimal IM for the entire transition states. This is especially convenient when performing risk assessment since it allows the use of directly available GMPEs.

Therefore, we proposed a global efficiency metric defined as

$$\beta_{\text{eff,glob}}(\text{IM}_i) = \min \left( \sum_{s=0}^S \frac{\beta_{\text{eff}}(\text{IM}_i)|_s}{\left( \sum_j^{41} \beta_{\text{eff}}(\text{IM}_j) \right) |_s} \right), \forall \text{IM}_i \in \text{IM} \text{ and } s = \{0, \dots, S\} \quad (9)$$

where  $s$  represents the allowable transition states, e.g., '0-0', '0-1', '0-2', '1-1', '1-2'. Specifically, we first normalize the  $\beta_{\text{eff}}$  index for each transition state over the  $i$  to 41 IMs. Then, we sum the same IM, across the transition states, and, finally, we select the minimum. [Table 4](#) gathers the global ranking for optimal IMs.

[Fig. 8](#) shows the probabilistic description of state-dependent fragilities as functions of the global optimal IM, i.e., the PGA. According to the definition of Eq. (1), [Fig. 8](#) reproduces the transition matrix of [Fig. 1\(a\)](#), i.e., the probabilities of transition to a specific  $DS_i$  state.

**Table 4**

Ranking of the optimal IMs according to the global  $\beta_{\text{eff,glob}}$ , defined in Eq. (9).

	Global optimal IM	$\beta_{\text{eff,glob}}$ index [%]
1.	PGA	9.12
2.	PGD	9.20
3.	E - ASA <sub>R800</sub>	9.21
4.	$I_{RG,a}$	9.39
5.	Sa( $T_1$ )	9.49

Specifically, in the first row, the probabilities of permanence in  $DS_0$  given  $DS_0$ , i.e.,  $\mathbb{P}_{00}$ , is defined as  $\mathbb{P}(DS = DS_0 | DS_0, IM) = 1 - \mathbb{P}_{01} - \mathbb{P}_{02}$ .

Here, particular attention is paid to the definition of  $\mathbb{P}_{01}$ , as also highlighted in the Figure by the \* character. Indeed, the  $\mathbb{P}_{01}$  is defined as the transition probabilities to attain  $DS_1$  only. This is different than the probabilities of exceedance  $DS_1$ , which implies the probabilities of attaining  $DS_1$  or worse, e.g.,  $DS_2$ , as reported for completeness and clarity in [Fig. A.8](#). The transition diagrams below each fragility clarify this by remarking only the allowable transitions. Similarly,  $\mathbb{P}_{02}$  is defined as the probability of reaching  $DS_2$ . There are no other worse conditions, since  $DS_2$  stands for the collapse case. Note a straightforward definition for the second row, since only two states are allowed. Particularly, in this row, an  $x$  marks the transition state associated with recovery processes, not addressed in this paper.

Finally, the last row of [Fig. 1\(a\)](#) is not included because represents the absorption case, i.e., the unit probability of collapse given collapse as initial conditions. Moreover, [Fig. 8](#) reveals a greater dispersion in the '0-2' curves with respect to the others. This is strictly related to the lower number of clustered data in this transition state. Indeed, the dispersion of fragilities is positively related to the number of clustered data that describes the fragilities functions.

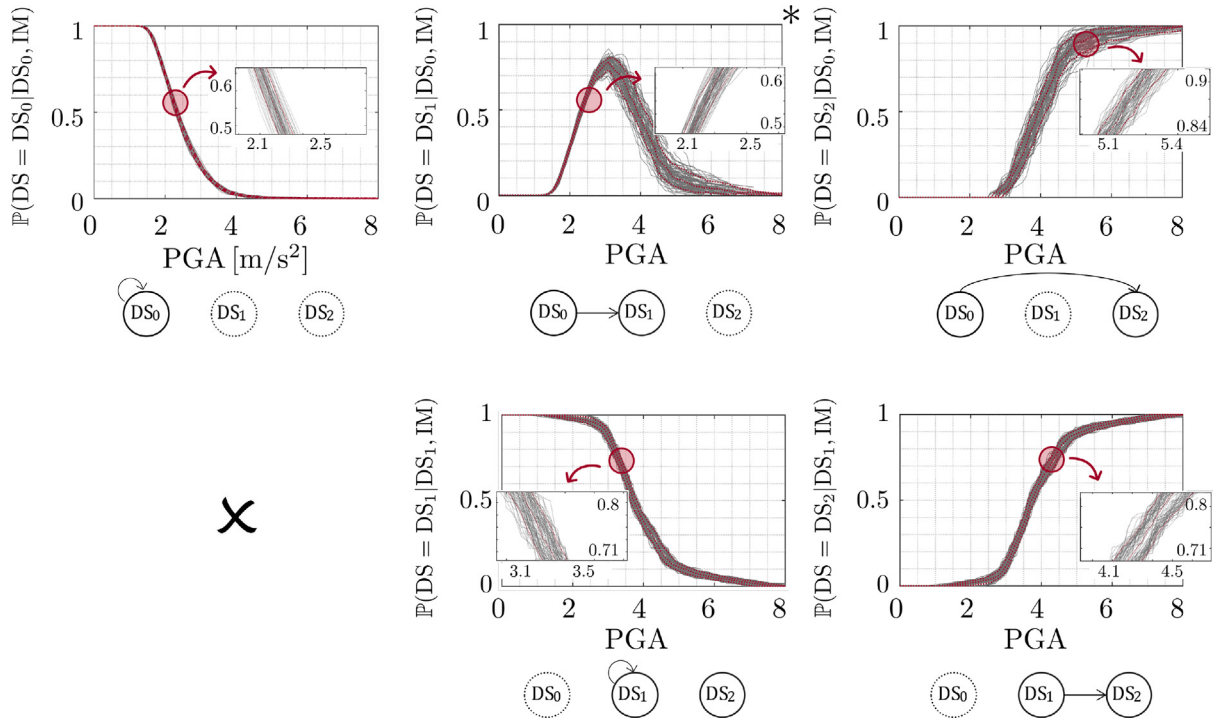


**Fig. 8.** Brute-force MCS state-dependent fragility functions, by means of PGA: grey lines represent single seed simulations; dashed-dot dark-red lines depict the 99% confidence bounds, whilst dashed-dark red ones the 50%. PGA is the IM adopted, according to the global optimal  $\beta_{\text{eff,glob}}$  among transition states. Notice that this Figure is in accordance with Eq. (1); therefore, the subplot at line 1 column 2 represents  $\mathbb{P}(\text{DS} = \text{DS}_1 | \text{DS}_0, \text{IM})$ . Therefore, this is not a commonly used “fragility function”, which reports the exceedance probability, i.e.  $\mathbb{P}(\text{DS} \geq \text{DS}_1 | \text{DS}_0, \text{IM})$ . [Appendix B](#) reports the commonly used fragility function.

### 3.3.2. Surrogate-based MCS for state-dependent fragility functions

To test the methodology of Section 2, surrogate models are developed for the MDof model, using as input the low dimensional representation of the seismic input, that is  $\widehat{\text{IM}}$ . Specifically, the predicted quantity is the ID-ratio, explicitly conditioned on two initial damage states: pristine and slightly damaged.

Accordingly, two independent surrogate models are developed to capture the ID-ratio under these distinct initial level conditions. Particularly, the PCE module of the opensource software UQLab [41] is adopted. PCE provides a functional approximation of the computational model  $\mathcal{M}(\widehat{\text{IM}})$  through its spectral representation on suitably built basis  $\psi_\alpha(\cdot)$  of polynomial functions, see the manual [42] for more details on the implementation. In real-world problems, due to limited computing power, the bases are truncated and the governing equation becomes:

$$\mathbf{y} \approx \mathcal{M}^{PCE}(\widehat{\text{IM}}) = \sum_{\alpha \in \mathcal{A}} c_\alpha \psi_\alpha(\widehat{\text{IM}}), \quad (10)$$

where  $\mathcal{A}$  is the set of selected multi-indices of multivariate polynomials and  $c_\alpha$  are the corresponding coefficients to be determined. The  $c_\alpha$  coefficients can then be calculated via projection, i.e., Gaussian or sparse quadrature, or regression methods, i.e., least-square algorithms. In this framework, we adopted the least-square method to determine the coefficients. Specifically, separated  $c_\alpha$  were estimated for each design of experiment  $D_s$ , constituted by the clustered pairs of pseudo-IMs and QoI of FE model response, i.e.,  $(\widehat{\text{IM}}; \mathcal{Y})$ , as:

$$c_\alpha = \underset{N_{D_s}}{\text{argmin}} \frac{1}{N_{D_s}} \sum_{i=1}^{N_{D_s}} \left[ y_i - \sum_{\alpha \in \mathcal{A}} c_\alpha \psi_\alpha(\widehat{\text{IM}}_i) \right]^2, \quad (11)$$

where  $N_{D_s}$  is the cardinality of the  $D_s$ ,  $s \in [\text{DS}_0; \text{DS}_1]$  denotes the initial damage state level of the design of experiment, and  $\{y^{(1)}, \dots, y^{(N)}\}$  the realizations of  $\mathcal{Y}$ . The choice of a least-square regression strategy is motivated by the possibility of adopting the bootstrap resampling method. This is particularly insightful when the size of the  $D_s$  is limited, since it allows the user to explore exhaustively the information on the

variability of the dataset. This can be achieved by first generating a set of bootstrap-resampled experimental design pairs  $(\widehat{\text{IM}}^{(b)}, \mathcal{Y}^{(b)})$  and then, by calculating a corresponding set of coefficients  $c_\alpha^{(b)}$ . Therefore, the response of each bootstrap PCE can be evaluated, yielding a family of  $b$  surrogate models that can be interpreted as trajectories. As recently explored in [43], this process of bootstrap-based trajectories resampling can be directly employed to assess the confidence bounds on surrogate-based estimators.

In this case, surrogates are developed for the two sets of initial damage state conditions, i.e.,  $\text{DS}_0$  (pristine) and  $\text{DS}_1$  (damaged) configurations. As recommended in [44], the subspace pursuit (SP) solver was deployed in the PCE metamodel. Nevertheless, to identify the most suitable way to calculate the coefficients  $c_\alpha$  of the PCEs, investigations were carried out on different sizes of the  $D_s$  and the vector of pseudo  $\widehat{\text{IM}}$ , describing the seismic input. Specifically, the vector of pseudo  $\widehat{\text{IM}}$  is defined as the  $n_{PCA}$  most significant PCA principal components.

$$\widehat{\text{IM}} = [\text{PC}_1, \text{PC}_2, \dots, \text{PC}_{n_{PCA}}]^T. \quad (12)$$

In [Appendix A.3](#), the scree plot of the PC results is reported. Since there is no notable increase in computational burden for choosing a high number of PCs, we opt for the first 10. More details on the correlations among IMs are discussed in the attached [Appendix A.2](#), along with histograms and inferred marginal distributions. To determine the optimal size of the design of experiment, three measures of errors on the performances of the PCE surrogates were used: (i) the relative generalization  $\epsilon_{\text{gen}}$ ; (ii) the leave-one-out  $\epsilon_{\text{LOO}}$ ; and (iii) the empirical  $\epsilon_{\text{emp}}$  error. In particular, the former

$$\epsilon_{\text{gen}} = \mathbb{E} \left[ (\mathcal{Y} - \mathcal{M}^{PCE}(\widehat{\text{IM}}))^2 \right] / \text{Var}[\mathcal{Y}] \quad (13)$$

is best suited if a validation set is available; otherwise, as it is commonly the case with expensive computational models, the other two are

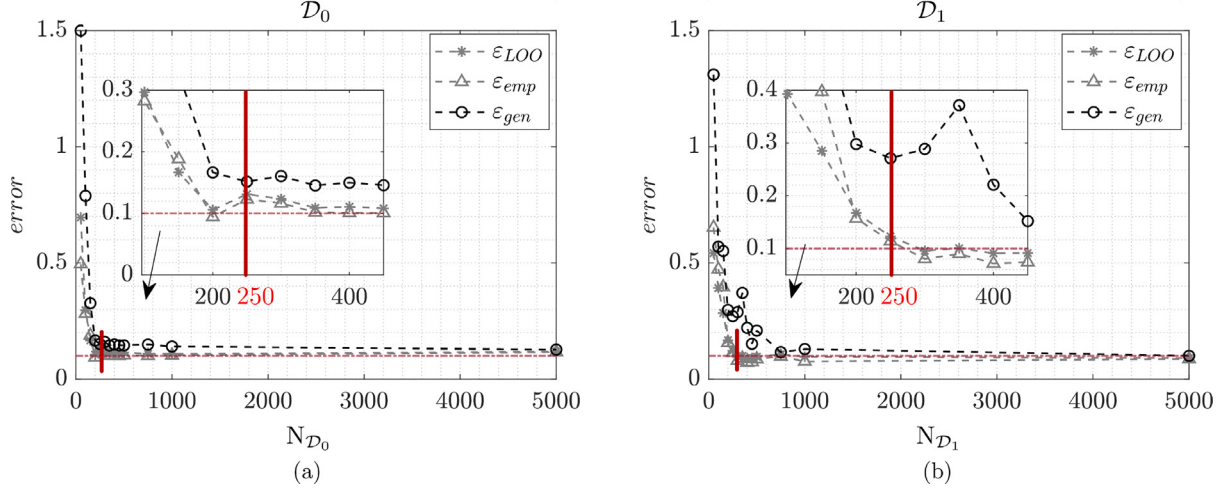


**Fig. 9.** Error plots considering the initial damage limit state (a)  $DS_0$ , namely design of experiment  $D_0$ , and the (b)  $DS_1$ , namely  $D_1$ . The error threshold is fixed to 0.10 and is represented by the red dotted horizontal line. In both datasets, the  $\epsilon_{LOO}$  and  $\epsilon_{emp}$  perform better than the  $\epsilon_{gen}$ , despite the vast validation set available in  $D_1$ , see Fig. 5(a).

preferred and evaluated with the following definition:

$$\epsilon_{LOO} = \frac{\sum_{i=1}^{N_{sims}} (y_i - \mathcal{M}^{PCE \setminus i}(\hat{\mathbf{m}}_i))^2}{\sum_{i=1}^{N_{sims}} (y_i - \hat{\mu}_Y)^2}, \quad (14)$$

$$\epsilon_{emp} = \frac{\sum_{i=1}^{N_{sims}} (y_i - \mathcal{M}^{PCE}(\hat{\mathbf{m}}_i))^2}{\sum_{i=1}^{N_{sims}} (y_i - \hat{\mu}_Y)^2}, \quad (15)$$

where  $N_{sims}$  is the total number of PCE-based MCS,  $y_i$  the realizations of  $\mathcal{Y}$ , and  $\hat{\mu}_Y$  is the sample mean of the design of experiment response. In addition, the bootstrap technique is applied to PCE to provide a local error estimator. Precisely, resampling with substitution is used on the  $D_s$ , thus generating a set  $B = 500$  bootstrap replications with the same number of sample points as the original  $D_s$ . Each  $b \in [1, B]$  replication is used to evaluate the corresponding PCE, yielding to  $b$  different sets of the PCE coefficients and predictions. Those  $b$  sets of responses are used to calculate the local variance and quantiles of the PCE predictor, exploiting all the information of the finite  $D_s$  size.

Fig. 9 shows the error trends against the  $D_s$  size. The results agree with the latest investigations reported in [44] concerning the ideal size of the design of experiment. Both the PCE-surrogate models for the  $D_0$  and  $D_1$  locate the optimal solution in 250 samples for the design of experiment dimension. Beyond this threshold, additional efforts to reduce model error result in marginal improvements or overfitting issues. Moreover, in this work, we employed the polynomial order  $p$ - and  $q$ -norm adaptivity algorithm in [44], within the basis-adaptive PCE framework of UQLab [41], allowing data-driven selection of the polynomial degree  $p$  and truncation order  $q$ . The optimal PCE model was then determined via the cross-validation error  $\epsilon_{LOO}$ , following the approach of Blatman and Sudret [45].

To ensure a comprehensive exploration of the polynomial basis, we allowed  $p$  and  $q$  to range over  $[1, 20]$  and  $[0.5, 1]$ , respectively, with the adaptive algorithm identifying the best combination directly from the data. The hyperbolic truncation scheme ( $q$ -norm constraint) was employed to promote sparsity while preserving dominant terms. For clarity, the  $q$ -norm is defined as  $\|\alpha\|_q = \left( \sum_{i=1}^M \alpha_i^q \right)^{1/q}$ , with  $M$  the dimension of the input.

As a result, the adaptivity algorithm converged to a polynomial degree 3 with  $\epsilon_{LOO} \approx 0.15$  for the undamaged  $D_0$  initial condition

converged. Fig. 10 reports the histograms and validation  $\mathcal{Y}_{D_0} - \mathcal{Y}_{PCE}$  plots. A validation set of  $10^4$  samples is deployed, thanks to the large number of simulations carried out on the MDof. A good agreement in terms of matching distributions between  $\mathcal{Y}_{D_0} - \mathcal{Y}_{PCE}$  is reached; also, samples-pairs are neatly aligned on the  $45^\circ$  line of the  $\mathcal{Y}_{D_0} - \mathcal{Y}_{PCE}$  plot, indicating a favourable performance. Similarly, for the damaged  $D_1$  initial condition of the system, the estimation of the PCE coefficients converged to a polynomial degree 3 with  $\epsilon_{LOO} \approx 0.14$ . Fig. 11 displays histograms of  $10^4$  samples for the  $\mathcal{Y}_{PCE}$  and FE  $\mathcal{Y}_{D_1}$  data. Again, since  $\mathcal{Y}_{D_1} - \mathcal{Y}_{PCE}$  pairs are well aligned to the  $45^\circ$  line, a good agreement is demonstrated.

Finally, state-dependent fragility curves are evaluated based on the results provided by the bootstrap PCE of both the pristine- $D_0$  and the damaged- $D_1$  datasets. As for the results of the brute-force MCS, fragilities are displayed referring to the optimal global IM. Thus, the  $\beta_{eff,glob}(IM_i)$  of Eq. (9) is evaluated for each transition state over the  $i$  to 41 IMs. Next, the global optimal  $IM^{**}$  is selected as follow  $IM^{**} = \operatorname{argmin}_{IM_i} \beta_{eff,glob}(IM_i)$ . Thus, Fig. 12 shows the state-dependent fragilities as functions of the global optimal  $IM^{**}$ , i.e., the PGA.

### 3.3.3. Validation of the framework

To facilitate a visual comparison, Fig. 13 presents the 99th confidence bounds for the transition states '0-1', '0-2', and '1-2' of the fragility functions derived using both brute-force MCS (benchmark case) and surrogate-based MCS. This provides a clear visual representation of the dispersions, allowing for an intuitive comparison between the median values and the variability of the fragility functions depicted in Figs. 8 and 12.

From a quantitative point of view, we measure the difference between the two fragility functions using the efficiency indices, the Kullback–Leibler (KL) divergence, and the Kolmogorov–Smirnov (KS) distance.<sup>3</sup> In particular, Table 5 gathers the  $\Delta(\beta_{eff})$  expressed as  $(|\beta_{eff}^{PCE} - \beta_{eff}|) / \beta_{eff}$  for each of the best indices of the transition states. The closer the delta is to 0, the better the matching of surrogate-based MCS with brute-force MCS results. It is generally observed that the  $\Delta(\beta_{eff})$  remains under the 0.20 threshold, which we consider, in this case, a good matching of responses.

<sup>3</sup> Technically speaking, the fragility functions are not proper CDFs, as the variable IM is in its conditional form. However, as they are assumed to be monotonically increasing, then they can be treated as CDFs, and the KL and KS distances are therefore used to assess the difference between the MCS and the PCE-based fragilities.

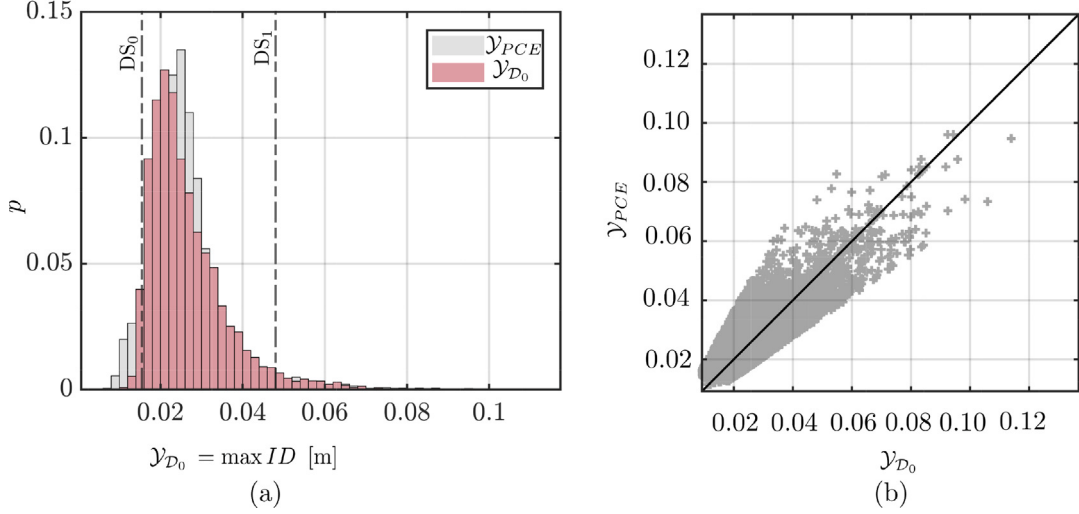


**Fig. 10.** (a) Comparison of the histograms for the outputs,  $\mathcal{Y}_{PCE}$ , of the PCE metamodel and the EDPs,  $\mathcal{Y}_{D_0}$ , of the  $D_0$  dataset, i.e., the initial damage state condition  $DS_0$ , and (b) the associated validation  $\mathcal{Y}_{D_0} - \mathcal{Y}_{PCE}$  plot. Limit state thresholds and  $\pm 1 \cdot \sigma$ , due to the uncertainties related to different initial damage conditions, are reported in the histograms of (a).

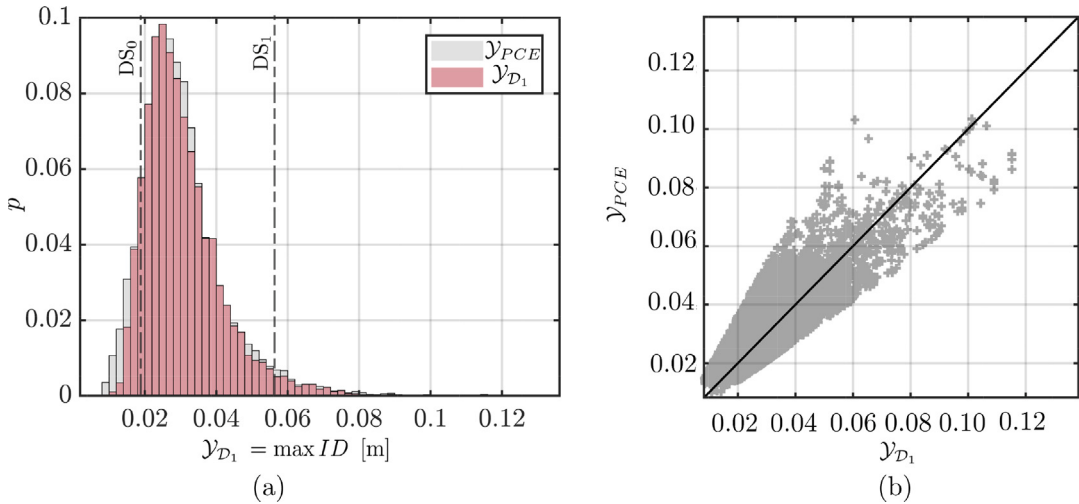


**Fig. 11.** (a) Comparison of the histograms for the outputs,  $\mathcal{Y}_{PCE}$ , of the PCE metamodel and the EDPs,  $\mathcal{Y}_{D_1}$ , of the  $D_1$  dataset, i.e., the initial damage state condition  $DS_1$ , and (b) the associated validation  $\mathcal{Y}_{D_1} - \mathcal{Y}_{PCE}$  plot.

**Table 5**

$\Delta(\beta_{\text{eff}})$  efficiency indices calculated as  $(|\beta_{\text{eff}}^{\text{PCE}} - \beta_{\text{eff}}|) / \beta_{\text{eff}}$  for the same top IMs for each transition states.

Frag. '0-0' optimal IM	$\Delta(\beta_{\text{eff}})$ index	Frag. '0-1' optimal IM	$\Delta(\beta_{\text{eff}})$ index	Frag. '0-2' optimal IM	$\Delta(\beta_{\text{eff}})$ index	Frag. '1-1' optimal IM	$\Delta(\beta_{\text{eff}})$ index	Frag. '1-2' optimal IM	$\Delta(\beta_{\text{eff}})$ index
PGA	0.12	$I_{RG,a}$	0.13	ASI	0.14	ASI	-0.17	E - ASA <sub>R80</sub>	0.07
IC	0.15	PGA	0.14	EPA	0.13	EPA	-0.19	E - ASA <sub>R200</sub>	0.08
$I_{RG,a}$	0.15	$I_{RG,v}$	0.16	RMS(ii)	0.15	PGA	-0.19	E - ASA <sub>R100</sub>	0.08
E - ASA <sub>R200</sub>	0.12	E - ASA <sub>R200</sub>	0.16	PGA	0.14	$I_{RG,v}$	-0.17	E - ASA <sub>R150</sub>	-0.08
RMS(ii)	-0.05	PGD	0.16	E - ASA <sub>R200</sub>	0.15	$I_{RG,a}$	-0.15	$I_{RG,a}$	-0.16

The KL divergence,  $D_{\text{KL}}(P \parallel Q)$ , quantifies how one probability distribution  $P$  is different from a second  $Q$ , defined on the same sample space. Specifically,  $P$  denotes the empirical probability distribution (Fig. 12); while  $Q$  represents the empirical probability distribution of

the mean brute-force MCS state-dependent fragilities (Fig. 8). Thus, KL is evaluated as provided in Eq. (16):

$$D_{\text{KL}}(P \parallel Q) = \sum_{x \in \mathcal{X}} P(x) \log \left( \frac{P(x)}{Q(x)} \right) \quad (16)$$

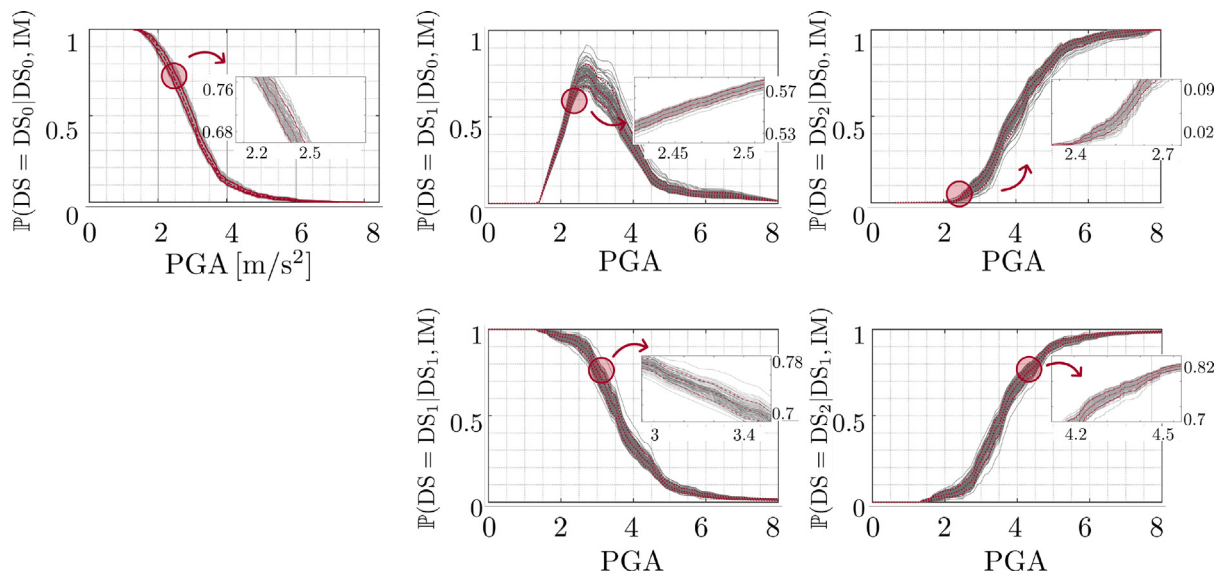


**Fig. 12.** Bootstrap-PCE-based MCS state-dependent fragility functions: grey lines represent single seed simulations; dashed-dotted dark red lines depict the 90% confidence bounds, whilst dashed-dark red ones the 50%.

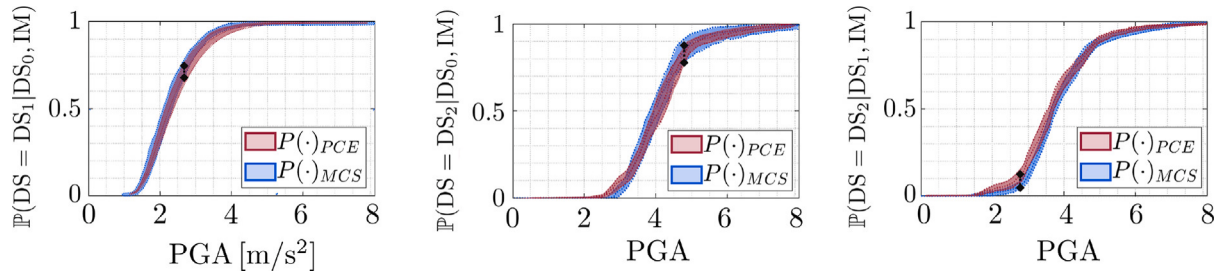


**Fig. 13.** PCE-based and brute-force MCS mean and 99th confidence bounds comparisons for the transition states '0-1', '0-2', and '1-2' with PGA as IM. Note that the probability of exceedance is adopted for the transition state '0-1'. The vertical lines mark the  $D_{KL}$  distances.

**Table 6**  
 $D_{KS}$  and  $D_{KL}$  measures for the mean PCE-based vs brute-force MCS state-dependent fragility functions.

	IM = PGA		
	'0-1'	'0-2'	'1-2'
$D_{KS}$	0.067	0.085	0.096
$D_{KL}$	0.164	0.200	0.186

where  $\mathcal{X}$  represents the sample space, that is, the domain of the optimal IM for each transition state. Fig. 13 shows the  $D_{KL}$  measure of the mean PCE-based and brute-force MCS state-dependent fragility functions for the transition states '0-1', '0-2', and '1-2'. As Table 6 shows, the  $D_{KL}$  distance is bounded  $\in [0.12 - 0.19]$ , meaning an overall good agreement (see [46]).

The KS distance is defined as:

$$D_{KS} = \sup_x |F_1(x) - F_2(x)|, \quad (17)$$

where  $F_1$  and  $F_2$  are the mean empirical cumulative distribution functions of the MCS brute-force and surrogate-based fragilities, respectively, and sup is the supremum function. Thus, Table 6 collects the results. The distance between the mean of the MCS brute-force functions and the surrogate-based is considered acceptable within the simulation framework. Moreover, fragilities must be integrated with the hazard curves; therefore, we consider these minimal differences as negligible.

#### 4. Industrial case: vertical tank installed on a 3D braced-frame structure

The above framework was applied to the SPIF #2 case study, [17, 20, 47]. Specifically, the object of the state-dependent fragility analysis was the vertical tank installed on the steel-BF industrial substructure.

##### 4.1. Step A—Computational model description

###### 4.1.1. FE physics-based model

We consider the FE model developed in the SAP2000® software [48] for the SPIF #2 experimental research campaign. Linear elastic elements were utilized in the modelling of the SPIF #2 structural system. Columns and beams were represented using Euler–Bernoulli beam elements, while floor diaphragms have been considered flexible. Consequently, non-rigid constraints were applied at each floor level. Concentrated masses were deployed to represent the weights of cabinets and tanks, which were incorporated into the model employing *ad-hoc* stick models. To account for joint stiffness, rotational links were implemented and calibrated based on experimental results obtained from prior phases of the project. Similarly, the Young's modulus for the structural elements was determined through calibration against previous test data, with a value of 220 GPa adopted for the analysis. Non-linearities were introduced to model the bracing system through non-linear tension only elements.

Fig. 14(a) shows the industrial substructure model tested on the shaking table. The mock-up consists of a full-scale 3-storey steel BF structure with flexible floors. Several NSCs of the industrial process

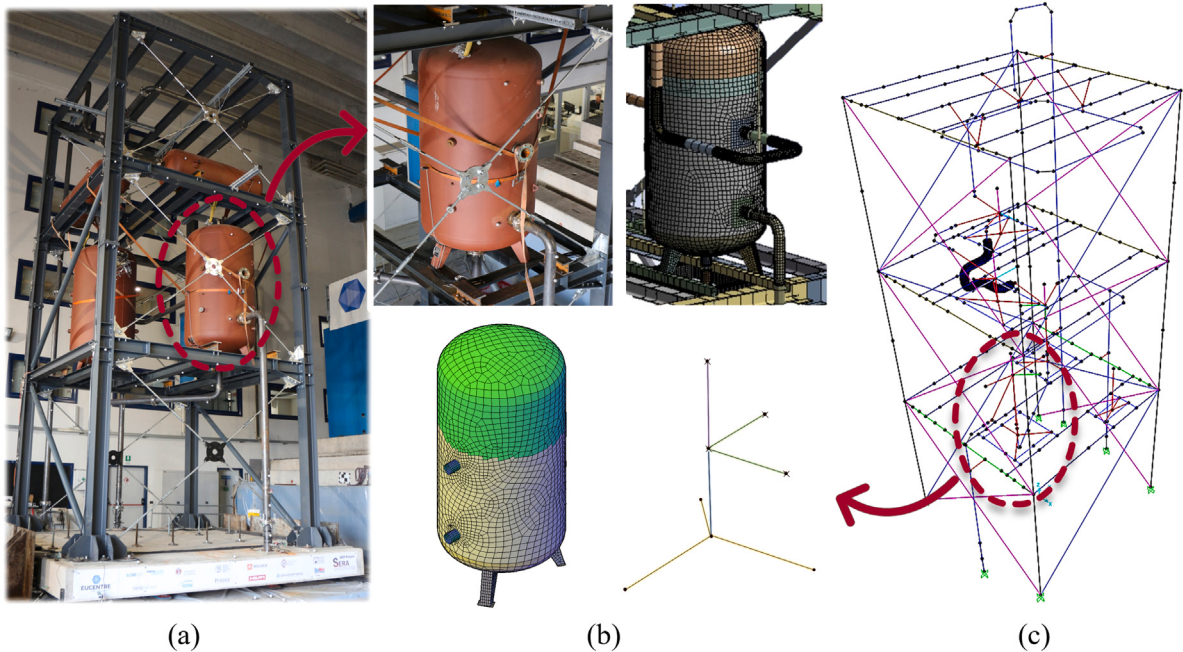


**Fig. 14.** The SPIF #2 mock-up: (a) photo of the braced frame (BF) configuration on the shake table of EUCENTRE Facilities and details of the vertical tank installed at the first level; (b) SAP2000® high-fidelity local FE model and *ad-hoc* implemented stick-model for the vertical tank; (c) global SAP2000® FE model of SPIF #2.

were installed, like tanks, cabinets, bolted flange joints, and T-joints. Particularly, the complex dynamic interaction between the main steel structure and one of the NSCs — the vertical tanks mounted on the first level — was examined. The strong displacement exhibited by those components deserved attention. This is because their damage can lead to severe consequences.

Fig. 14(b) highlights the investigated vertical tank and shows a detail of the *ad-hoc* designed stick model for the tanks, along with its expensive reference high-fidelity local FE model. The stick model was developed with the goal to: (i) mimic the modal properties and (ii) catch the different effects of the participating seismic mass on the supporting girders system. The latter is particularly delicate since the participating mass varies with the intensity level of the seismic excitation. A thorough discussion on FE modelling and calibration of the global SPIF #2 model of Fig. 14(c) is reported in [17]. The shake table tests showed that the vertical tanks were one of the most critical elements among the installed components. Therefore, we developed fragility analysis for these elements, using the bootstrap PCE technique of the previous Section.

#### 4.2. Step B—Input definition

The framework outlined in Section 2 is adopted. Sequences of seismic events were assigned to the FE model of SPIF #2 to (i) simulate different damage initial configurations and (ii) cover each transition state. To determine the number of training samples, preliminary analyses were conducted to evaluate the response of the system under varying numbers of ground motions within the same seismic sequences. As a result, a total of 100 gms sequences of 5 earthquakes, as opposed to the 10 used in the MDOF case study, were implemented by the same ensemble of gms generated by the GMM of Section 3.2. The computational cost pro single sequential NLTHA is ~30 min on an Intel(R) Core(TM) i9-10900K CPU @3.70 GHz, 10 Core(s) —128 GB RAM. This choice was driven by a trade-off between computational efficiency and a well-defined population of the transition matrix of Fig. 1(a). The transition matrix for the vertical tank was defined on two performance limit states, e.g., DS<sub>1</sub> and DS<sub>2</sub>. Those were set according to

literature recommendations, see [49], and confirmed by the experimental campaign, see [17]. The first, DS<sub>1</sub>, is the design basis earthquake (DBE), which is linked to the operation and functionality of the process plant. The second, DS<sub>2</sub>, is the safe shutdown earthquake (SSE) limit state, for which the fundamental safety functions can be ensured with minor damages, although the facility is no longer operational. Thresholds were experimentally identified by maximum acceleration values recorded at the base of the vertical tank

$$\max |\ddot{u}_{\text{base}}^{\text{v.tank}}| = \begin{cases} 10 \text{ m/s}^2, & \text{DBE (DS}_1\text{)} \\ 16 \text{ m/s}^2, & \text{SSE (DS}_2\text{)} \end{cases} \quad (18)$$

for the DBE and SSE, respectively, as reported in [17].

#### 4.3. Step C—QoI response

##### 4.3.1. NLTHAs and experimental design generation

As illustrated in Fig. 2, the results of the NLTHAs performed on the FE model were clustered into the transition states of Fig. 1(a). Specifically,  $D_0$  indicates the dataset associated with pristine initial damage conditions, whilst  $D_1$  denotes the dataset for which the threshold associated with the DBE limit state was exceeded. Lastly,  $D_2$  collects the results of simulations for which the SSE limit state was attained. As Fig. 15 shows, almost 47% of the simulations belong to the  $D_0$  damage state initial condition. Particularly, 13% and 7% transitioned from undamaged initial conditions to exceeding the DBE and SSE threshold at the end of the NLTHAs, respectively. Instead, 38% of simulations belong to  $D_1$ , out of which 16% stayed in the same damage level even after other seismic shocks. Finally, 15% of the simulations reached the absorption state. Again, the 41 IMs of Table A.1 were evaluated for each gms of the NLTHA simulations. PCA was then applied to reduce the order of the input dimension. Specifically, 10 PCs were used to cover 99% of the variability of data.

##### 4.3.2. PCE metamodeling

State-dependent fragilities required many more analyses than the ones performed on the computationally intensive FE model. In this case study, the predicted QoI is the maximum acceleration at the base of the vertical tank, conditioned on either the pristine condition or the

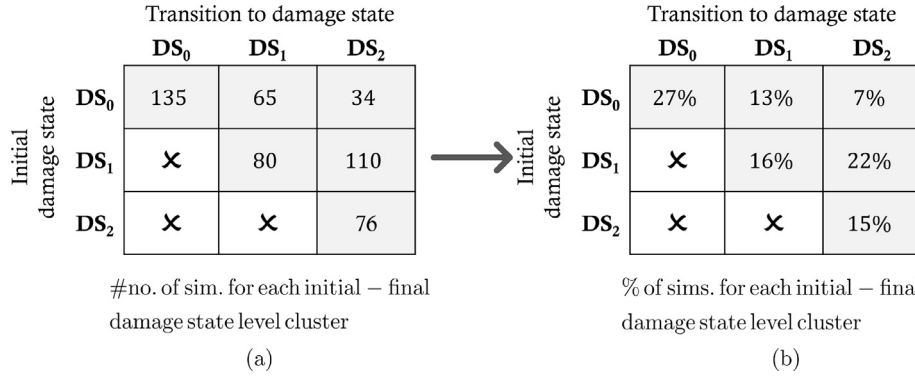


Fig. 15. Transition state matrices for the SPIF #2: (a) counters and (b) percentages of simulation for each initial–final damage state level cluster, respectively.

operability and functionality of the industrial plant processes. Thus, two separate PCE metamodels were implemented to overcome the computational and time issues. Specifically, the first metamodel was built on the experimental design  $D_0$  of simulations belonging to the pristine initial condition dataset. The second on the  $D_1$ , the family of simulations with initial conditions attaining the DBE limit state. Resampling with substitution was used on both the experimental design  $D_{0,1}$ , thus generating sets of bootstrap replications to estimate confidence bounds. A total number of replications  $B = 500$  is considered.

As in the previous case study, the  $p$ - and  $q$ -norm adaptivity algorithm is used with parameter ranging between [1,20] and [0.5,1], respectively. Based on the latest findings of [44], the subspace pursuit (SP) solver was adopted with 10 PCs. Here, the set of orthogonal polynomials is constructed in UQLab by means of the so-called Stieltjes procedure, as implemented by default in the UQLab PCE module [42]. The procedure is a recursion-formula-based version of classical functional Gram–Schmidt for polynomials. Indeed, the joint distribution of the input, i.e., the PC coefficients of the  $\widehat{\mathbf{IM}}$ , is estimated via maximum likelihood to a large set of marginal distributions, enforcing independence between components. Each marginal distribution is then selected according to its Akaike information criterion (AIC) score, to select the best model. This procedure is described in detail in the [50].

As a result, Fig. 16(a) reports the histogram of the surrogate predictor over the histogram distribution of the  $D_0$ . The limit state thresholds of DBE and SSE are also reported. A favourable performance is attained, with a final  $\epsilon_{\text{LOO}}$  error of 4.17E–02. The estimation of bootstrap PCE coefficients converged to a polynomial degree order of 3.

Moreover, Fig. 16(b) shows the control  $\mathcal{Y}_{D_0} - \mathcal{Y}_{\text{PCE}}$  plot: a good alignment is found with the 45° line, which represents the ideally perfect match between true and surrogate data.

Similarly, bootstrap PCE was performed for the experimental design  $D_1$ . As a result, Fig. 17(a) reports the histogram distribution of both the  $\mathcal{Y}_{\text{PCE}}$  predictor and the  $\mathcal{Y}_{D_1}$  data of the damaged initial state condition. A generally good agreement is found, with a few exceptions in the range between [21–22] m/s<sup>2</sup>. This is reflected also in the control plot  $\mathcal{Y}_{\text{PCE}} - \mathcal{Y}_{D_1}$  of Fig. 17(b), where the dispersion is greater in that range. The estimation of the PCE coefficients converged at a polynomial degree of order 5 with a final  $\epsilon_{\text{LOO}}$  error of 4.73E–02.

#### 4.4. Fragility assessment

Following Section 3, a global optimal IM descriptor for the derivation of fragility functions is evaluated. Table 7 gathers the ranking of the first five minimum  $\beta_{\text{eff,glob}}$  for the SPIF case study, derived by Eq. (9). It emerges that IMs strictly correlated with acceleration or energy content are the most suitable for the case study. Next, we select PGA as the optimal IM and compute state-dependent fragilities using PCE-surrogate models as described in Section 2.

Table 7  
Ranking of the optimal IMs according to the global  $\beta_{\text{eff,glob}}$ , defined in Eq. (9).

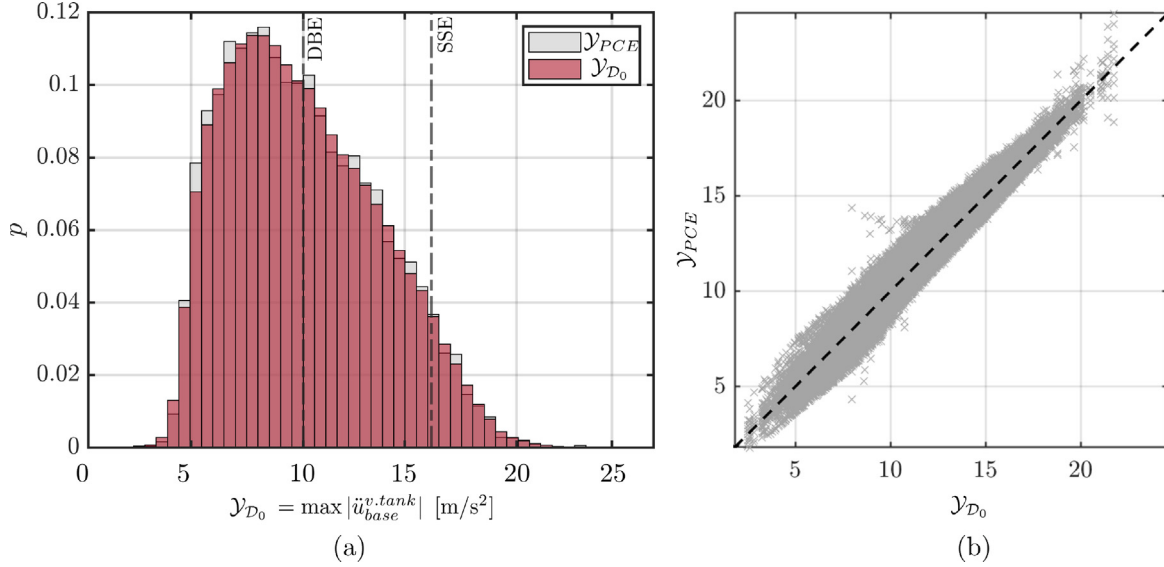
	Global optimal IM	$\beta_{\text{eff,glob}}$ index [%]
1	PGA	4.02
2	E <sub>cum</sub>	4.35
3	I <sub>A</sub>	5.07
4	I <sub>F</sub>	5.31
5	I <sub>RG,a</sub>	7.42

Fig. 18 shows the probabilistic description of state-dependent fragilities as functions of the PGA. The curves representing the 1%–50%–99% percentiles are displayed with black-dotted thick lines, whilst the 10%–90% with red-dotted lines, and their area with darker to lighter red-shaded colours.

In Appendix C, we report the collection of state-dependent fragility functions based on the optimal  $\beta_{\text{eff}}$  index for each transition state in Fig. C.1. Moreover, the commonly referred fragility functions as the probability of exceedance of a certain threshold, in this case, the DS<sub>1</sub> threshold given DS<sub>0</sub> initial damage condition, is reported in Fig. C.2.

## 5. Conclusions and future developments

An innovative, non-intrusive UQ-based framework for assessing state-dependent fragility functions has been proposed. The framework builds on a stochastic representation of seismic sequences, calibrated and validated FE models, principal component analysis (PCA) representation of the input, and advanced polynomial chaos expansion (PCE)-based surrogate modelling. The proposed framework provides for both vast flexibility and integration with FEM experts as well as extreme computational efficiency. State-dependent fragility analysis requires a vast number of NLTHAs, based on time series of stochastic seismic sequences. However, when considering realistic computational models, the significant computing demands of an extensive set of sequential NLTHAs generally hinder this direct derivation of state-dependent fragilities. Hence, we propose an innovative UQ-based framework that combines a PCA representation of the stochastic input and an advanced PCE surrogate modelling of the QoI of the system. Specifically, we first performed a reduced number of stochastic seismic sequence NLTHAs on computationally intensive FEM. Next, the resulting QoIs were clustered according to predefined damage initial states. At the same time, we performed PCA on the exhaustive vector of  $\widehat{\mathbf{IM}}$ , to obtain a low-dimensional input representation of the time series sequences  $\widehat{\mathbf{IM}}$ . Next, on the pairs of clustered QoIs and the  $\widehat{\mathbf{IM}}$ —i.e., the design of experiment—, we built different PCE surrogate models, one for each initial damage state of the system. Successively, the vast number of MCS surrogate-based analyses enabled us to derive non-parametric



**Fig. 16.** (a) Histogram distribution of the PCE surrogate  $\mathcal{Y}_{PCE}$  (light grey) predictor vs the  $\mathcal{Y}_{D_0}$  original data of the initial undamaged condition dataset; (b) control plot of the performance of the  $\mathcal{Y}_{PCE}$  surrogate model vs the  $\mathcal{Y}_{D_0}$  reference experimental design samples.

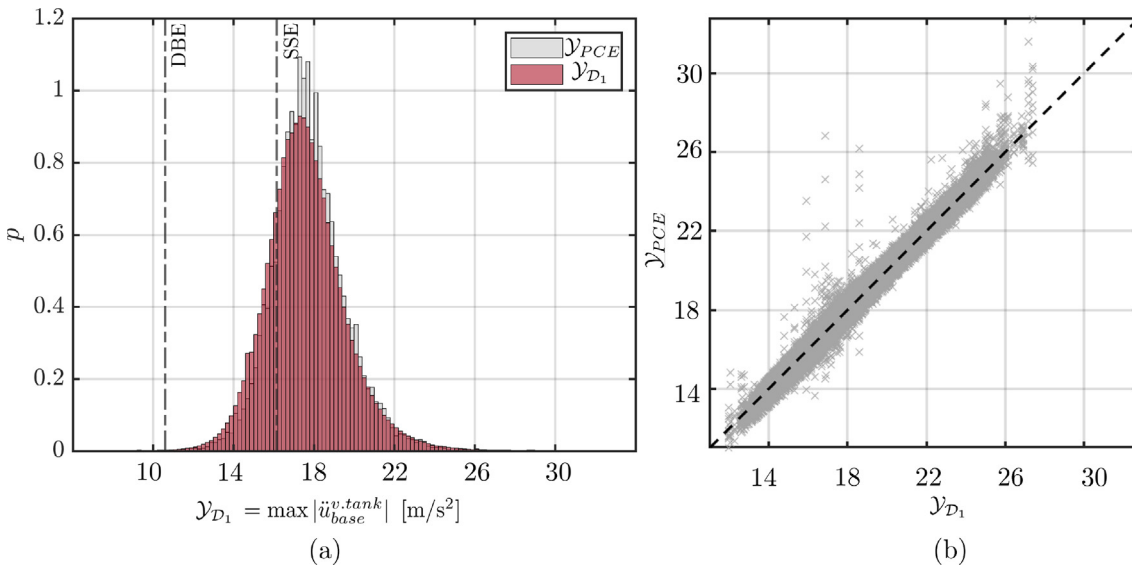


**Fig. 17.** (a) Histogram distribution of the PCE surrogate  $\mathcal{Y}_{PCE}$  (light grey) predictor vs the  $\mathcal{Y}_{D_1}$  original data of the initial undamaged condition dataset; (b) control plot of the performance of the  $\mathcal{Y}_{PCE}$  surrogate model vs the  $\mathcal{Y}_{D_1}$  reference experimental design samples.

state-dependent fragility functions. In particular, the UQ-based framework was applied twice. First, it was tested and validated on a simple yet realistic 2D MDof system endowed with Bouc–Wen hysteresis. Specifically, given the computationally efficient benchmark case study, state-dependent fragilities were evaluated both via the MCS brute-force method and the MCS PCE-based one. Global and local efficiency  $\beta_{\text{eff}}$  indices for each transition states were evaluated to determine the optimal IM for fragility assessment. Moreover, qualitative and quantitative comparisons through  $\Delta\beta_{\text{eff}}$  and statistical measures confirmed the acceptable performance of the developed framework. Second, the validated methodology was applied to derive seismic state-dependent fragility functions for an industrial process component. Specifically, the critical vertical tank of the 3-storey 3D BF industrial mock-up of project SPIF #2 was considered. Following the previous example, a given

number of sequences of synthetic ground motions were assigned as input for NLTHAs on the refined FEM of the coupled SPIF system. Then, clustering of the QoIs along with PCA for dimensionality reduction of the stochastic seismic sequences of the input was performed. Next, PCE surrogate models were built for the identified initial damage state conditions. Moreover, MCS PCE-based state-dependent fragility functions were evaluated. Thus, the developed framework allows to unlock the possibility of efficiently computing state-dependent fragility for a variety of problems. In addition, the versatility of the framework allows us to extend it to a vector of IMs for fragility assessment, in the future. The use of the framework for aftershock sequences is being considered as a second future direction, provided with a stochastic representation of input sequences. Finally, either the single state-dependent fragility function or the entire framework can be used to estimate seismic risk.

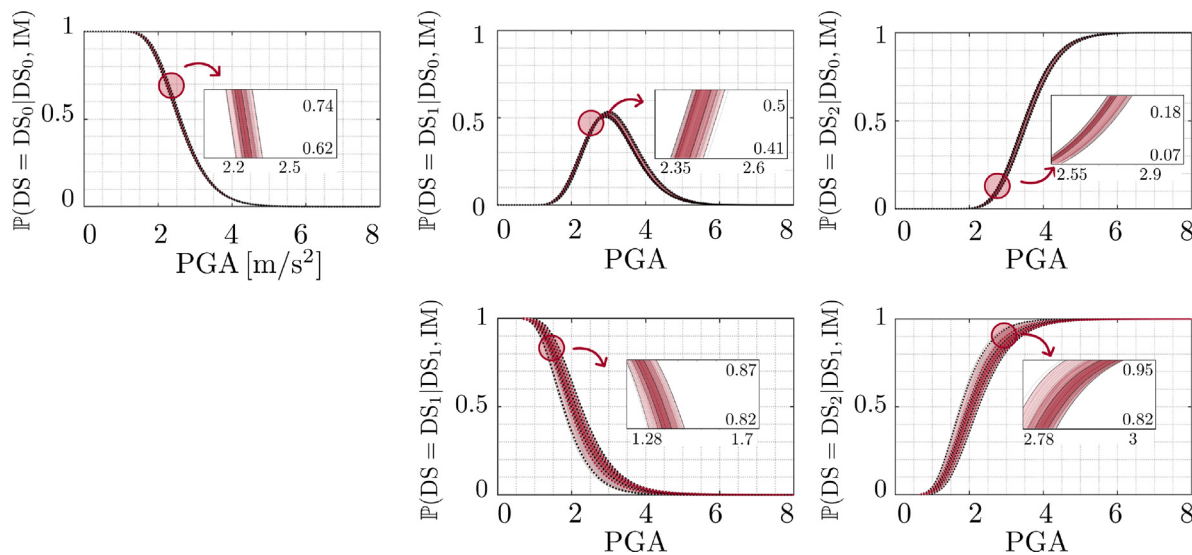


**Fig. 18.** Bootstrap-PCE state-dependent fragility curves of the SPIF #2 vertical tank: black-dotted thick lines stand for the 1%, 50%, and 99% percentiles. Red-dotted lines for the 10% and 90% percentiles, along with darker to lighter red-shaded colours.

#### CRediT authorship contribution statement

**Chiara Nardin:** Writing – original draft, Validation, Methodology, Formal analysis, Software, Data curation, Conceptualization. **Stefano Marelli:** Writing – review & editing, Supervision, Software, Methodology, Data curation, Conceptualization. **Oreste S. Bursi:** Review & editing, Supervision, Funding acquisition . **Bruno Sudret:** Supervision, Methodology, Funding acquisition . **Marco Broccardo:** Writing – review & editing, Validation, Supervision, Methodology, Funding acquisition, Conceptualization.

#### Declaration of competing interest

The authors declare that they have no known competing financial interests or personal relationships that could have appeared to influence the work reported in this paper.

#### Acknowledgements

The research leading to these results has received funding from (i) the European Community's "NextGeneration EU Programme" [PRIN - 2022MJ82MC 001 - CUPE53D23004440006] - for the first and the last author; (ii) the National Project MUR PNRR M4C2-CN1-SPOKE 9 - for the third author; (iii) the Italian Ministry of Education, University and Research (MIUR) in the frame of the "Departments of Excellence 2023-2027" (grant L232/2016) - for the third and the last author; and (iv) the Marie-Sklodowska Curie program and the REACTIS project, GA no.101147351 for the first author. Views and opinions expressed are however those of the authors only and do not necessarily reflect those of the European Union, or REA or any sponsor. Neither the European Union nor the granting authority can be held responsible for them.

#### Appendix A. - Input support material

##### A.1. IM parameters

Besides the most popular IMs such as PGA and PGV, novel and less widespread IMs have also been introduced. Among them: the  $I_{RG,a}$  Riddell–Garcia Intensity acceleration and velocity measures, which minimize dispersion of hysteretic energy-dissipation spectra of inelastic systems; the  $I_F$  Fajfar Intensity, a compound IM that takes into account

the damage capacity of medium-period structures; and the  $E - ASA_{R,x}$  equipment relative average spectral acceleration, introduced in [19]. The last one is of particular interest since it allows us to consider shifts in the frequency range of the structure due to damage experienced by the installed equipment.

##### A.2. Histograms and distributions of the input

**Fig. A.1** illustrates the correlation among the IM parameters, which varies  $[-1, +1]$ . It emerges:

- high correlations among  $E - ASA_{R,x}$ ,  $Sa$  and  $E - ASA_{R,x}$  as the frequency drop  $R_x$  increases - indexes from 36 to 41;
- significative correlations among IMs sensitive to acceleration EPA - idx. 30 -,  $ASA_{40}$  - idx. 28, and  $ASI$  - idx. 29;
- negative correlations or low correlations for the significant time duration  $T_d$  - idx. 23, the Cosenza-Manfredi intensity  $I_{CM}$  - idx. 27 - and both the frequency-related IMs mean  $F_m$  - idx. 33 - and rate of change mean frequencies  $\dot{F}_m$  - idx. 34;
- linear correlations between  $Sa - Sv$  and  $Sv - Sd$  - idxs. 4–18, as expected by the definitions.

**Table A.2** and **Figs. A.2–A.6** gather the histograms and inferred pdf for each IM presented in **Table A.1** of Section 3.2.

##### A.3. PCA of the input

**Fig. A.6** reports the variability covered by increasing the number of PCs through a scree plot. As one can notice, the first 3 PCs are sufficient to describe more than the 80% of the input data, 6 PCs the 90% and 10 PCs are needed to get the 99% of the input variance.

To highlight which and how each  $im_i$  contributes to PCs, the first three PCs are displayed on the biplots in **Fig. A.8**. Particularly, in **Fig. A.8**, only the relevant IMs—i.e., the ones that present high scores—are plotted and labelled with the corresponding number ID of **Table A.1**. Therefore, the information provided is twofold: (i) on the correlation among IMs; (ii) on the magnitude of the importance of the IMs in the definition of PCs. For instance, for  $PC_2$ : almost all the plotted IMs are positively correlated with  $PC_2$  itself. The 33-IM, i.e.,  $F_m$ , represent the exception, since it is in the opposite direction with  $PC_2$ , thus entailing a negative association. The positive/negative correlations and the order of magnitude are summarized in the coordinates of the PCs next to the biplot, until the tenth coefficient.

**Table A.1**  
A comprehensive list of ground motion IM parameters [19]–[39].

No.	Description of IM	Symbol	Units	Mathematical model
1	Peak ground acceleration	PGA	[m/s <sup>2</sup> ]	$\max( \ddot{u}(t) )$
2	Peak ground velocity	PGV	[m/s]	$\max( \dot{u}(t) )$
3	Peak ground displacement	PGD	[m]	$\max( u(t) )$
4,...,8	Spectral displacement	Sd	[m]	$S_d(T_x)$
9,...,13	Spectral velocity	Sv	[m/s]	$S_v(T_s)$
14,...,18	Spectral acceleration	Sa	[m/s <sup>2</sup> ]	$S_a(T_x)$
19	Arias intensity	I <sub>A</sub>	[m/s]	$\pi/2 g \cdot \int_0^{T^*} a^2(t) dT$
20	Total cumulative energy	E <sub>cum</sub>	[m <sup>2</sup> /s <sup>3</sup> ]	$\int \dot{u}^2(t) dt$
21	Riddell–Garcia Intensity Acceleration	I <sub>RG,a</sub>	[m/s <sup>5/3</sup> ]	$(PGA)^{+1} \cdot (T_d)^{+1/3}$
22	Riddell–Garcia Intensity Velocity	I <sub>RG,v</sub>	[m <sup>2/3</sup> /s <sup>1/3</sup> ]	$(PGV)^{+2/3} \cdot (T_d)^{+1/3}$
23	Significant time duration	T <sub>d</sub>	[s]	$t_{95} - t_{05}$
24	Root mean square of acceleration	RMS ( $\ddot{u}(t)$ )	[m/s <sup>2</sup> ]	$\sqrt{\frac{1}{N} \sum_{n=1}^N  \ddot{x}_N ^2}$
25	Characteristic intensity	IC	[m <sup>3/2</sup> /s <sup>3/2</sup> ]	$RMS(\ddot{u}(t))^{1.5} \cdot T_d^{0.5}$
26	Cumulative absolute velocity	CAV	[m/s]	$\int_0^{T^*}  a(t)  dt$
27	Cosenza–Manfredi Intensity	I <sub>CM</sub>	[–]	$2g/\pi \cdot (PGA)^{-1} (PGV)^{-1} (AI)^{+1}$
28	Average spectral acceleration	ASA <sub>40</sub>	[m/s]	$2.5/f_1 \int_{0.6 \cdot f_1}^{f_1} S_a(f, \epsilon) df$
29	Acceleration spectral intensity	ASI	[m/s <sup>2</sup> ]	$f_{0.1}^{0.5} S_a(T, \epsilon) dT$
30	Effective peak acceleration	EPA	[m/s <sup>2</sup> ]	$1/2.5 \int_{0.1}^{2.5} S_a(T, \epsilon) dT$
31	Velocity to acceleration ratio	I <sub>v/a</sub>	[s]	$PGV/PGA$
32	Fajfar Intensity	I <sub>F</sub>	[m/s <sup>3/4</sup> ]	$(PGV)^{+1} \cdot (T_d)^{+1/4}$
33	Mean frequency	F <sub>m</sub>	[1/s]	$\sum_i U_i^2(f_m)/\sum_i U_i^2$
34	Rate of change mean frequency	F̄ <sub>m</sub>	[–]	$dF_m(T)/dT$
35	Fourier amplitude spectrum area	FAS <sub>area</sub>	[m/s <sup>2</sup> ]	$\frac{1}{4df} \int_{f_1-2df}^{f_1+2df} U(f) df$
36,...,41	Equipment relative average spectral acceleration	E – ASA <sub>R<sub>x</sub></sub> <sup>**</sup>	[m/s <sup>2</sup> ]	$\frac{1}{f_1 \cdot (X_f - 1)} \cdot \int_{f_1}^{X_f \cdot f_1} S_a(f, \epsilon) df$

\* where  $T^* \in [0.50; 0.35; 0.25; 0.15; 0.10]$ .

\*\* R indicates the chosen percentage of drop of the fundamental frequency ( $X_f = 1 - (R/100)$ ); R ∈ [40; 67; 80; 100; 150; 200].

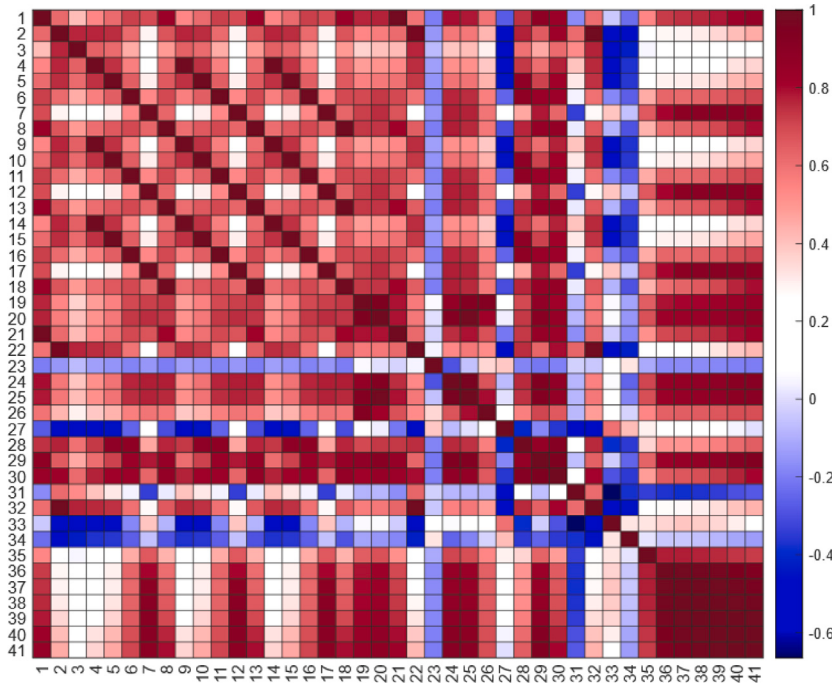


**Fig. A.1.** Correlation map between input IM parameters.

**Table A.2**

Histograms and distributional models inferred for each IM.

Index	Name	Type	Parameters	Moments
1	PGA	Gumbel	2.027e+00, 6.236e-01	2.387e+00, 7.998e-01
2	PGV	Gumbel	1.408e-01, 5.683e-02	1.736e-01, 7.289e-02
3	PGD	Gamma	3.853e+01, 3.489e+00	9.055e-02, 4.848e-02
4	Sd(T <sub>1</sub> )	Gumbel	1.447e-02, 6.679e-03	1.833e-02, 8.566e-03
5	Sd(T <sub>2</sub> )	Gumbel	1.031e-02, 4.263e-03	1.277e-02, 5.468e-03
6	Sd(T <sub>3</sub> )	Gumbel	7.792e-03, 2.635e-03	9.313e-03, 3.379e-03
7	Sd(T <sub>4</sub> )	LogNormal	-5.551e+00, 3.517e-01	4.133e-03, 1.500e-03
8	Sv(T <sub>5</sub> )	LogNormal	-6.831e+00, 3.239e-01	1.137e-03, 3.782e-04
9	Sv(T <sub>1</sub> )	Gumbel	1.814e-01, 8.370e-02	2.297e-01, 1.074e-01
10	Sv(T <sub>2</sub> )	Gumbel	1.835e-01, 7.591e-02	2.274e-01, 9.736e-02
11	Sv(T <sub>3</sub> )	Gumbel	1.958e-01, 6.622e-02	2.341e-01, 8.493e-02
12	Sv(T <sub>4</sub> )	LogNormal	-1.815e+00, 3.517e-01	1.732e-01, 6.285e-02
13	Sv(T <sub>5</sub> )	LogNormal	-2.690e+00, 3.239e-01	7.156e-02, 2.380e-02
14	Sa(T <sub>1</sub> )	Gumbel	2.273e+00, 1.049e+00	2.878e+00, 1.345e+00
15	Sa(T <sub>2</sub> )	Gumbel	3.268e+00, 1.352e+00	4.048e+00, 1.733e+00
16	Sa(T <sub>3</sub> )	Gumbel	4.922e+00, 1.664e+00	5.883e+00, 2.134e+00
17	Sa(T <sub>4</sub> )	LogNormal	1.920e+00, 3.517e-01	7.260e+00, 2.634e+00
18	Sa(T <sub>5</sub> )	LogNormal	1.452e+00, 3.239e-01	4.502e+00, 1.497e+00
19	I <sub>A</sub>	LogNormal	-6.729e-01, 5.712e-01	6.006e-01, 3.730e-01
20	E <sub>cum</sub>	LogNormal	1.342e+00, 5.453e-01	4.439e+00, 2.612e+00
21	I <sub>RG,a</sub>	Gumbel	4.151e+00, 1.222e+00	4.856e+00, 1.567e+00
22	I <sub>RG,v</sub>	LogNormal	-5.098e-01, 2.745e-01	6.237e-01, 1.745e-01
23	T <sub>d</sub>	Gaussian	8.696e+00, 1.637e+00	8.696e+00, 1.637e+00
24	RMS( $\ddot{u}(t)$ )	LogNormal	-7.590e-01, 2.845e-01	4.875e-01, 1.415e-01
25	IC	LogNormal	-6.627e-02, 4.070e-01	1.017e+00, 4.315e-01
26	CAV	Gamma	9.262e-03, 9.638e+00	1.041e+03, 3.352e+02
27	I <sub>CM</sub>	LogNormal	2.178e+00, 4.817e-01	9.915e+00, 5.067e+00
28	ASA <sub>40</sub>	Gamma	1.122e-01, 8.580e+00	7.647e+01, 2.611e+01
29	ASI	LogNormal	6.025e+00, 2.910e-01	4.315e+02, 1.283e+02
30	EPA	Gamma	4.737e-02, 1.134e+01	2.393e+02, 7.108e+01
31	I <sub>v/a</sub>	Gamma	1.343e+02, 9.941e+00	7.400e-02, 2.347e-02
32	I <sub>F</sub>	Gumbel	2.407e-01, 9.524e-02	2.957e-01, 1.221e-01
33	F <sub>m</sub>	Gaussian	4.649e+00, 4.801e-01	4.649e+00, 4.801e-01
34	F̄ <sub>m</sub>	GumbelMin	-2.667e-04, 2.347e-04	-4.022e-04, 3.011e-04
35	FAS <sub>area</sub>	Exponential	3362	2.974e-01, 2.974e-01
36	E - ASA <sub>40</sub>	LogNormal	2.371e+00, 3.504e-01	1.138e+01, 4.115e+00
37	E - ASA <sub>R<sub>67</sub></sub>	LogNormal	3.283e+00, 3.387e-01	2.823e+00, 9.842e+00
38	E - ASA <sub>R<sub>80</sub></sub>	LogNormal	3.561e+00, 3.325e-01	3.719e+01, 1.271e+01
39	E - ASA <sub>R<sub>100</sub></sub>	LogNormal	3.917e+00, 3.229e-01	5.296e+01, 1.756e+01
40	E - ASA <sub>R<sub>150</sub></sub>	LogNormal	4.495e+00, 3.110e-01	9.398e+01, 2.995e+01
41	E - ASA <sub>R<sub>200</sub></sub>	LogNormal	4.879e+00, 3.056e-01	1.378e+02, 4.313e+01

**Appendix B. - MDof support material**

In this note, the  $P_{01}$  is defined as the transition probabilities to exceed DS<sub>1</sub>, which implies the probabilities of attaining DS<sub>1</sub> or worse, e.g., DS<sub>2</sub>. This is different than the probabilities to attain DS<sub>1</sub> only, as reported in the main text of the article.

**Appendix C. - SPIF #2 support material****C.1. Collection of the optimal state-dependent functions for each transition state**

The optimal IMs for each transition state were determined according to the  $\beta_{\text{eff}}$  index of Eq. (8). Table C.3 collects the top-five-ranked IMs for each transition state.

It is possible to notice that the Fajfar intensity I<sub>F</sub>, the equipment relative average spectral acceleration E - ASA<sub>R<sub>67</sub></sub>, and the cumulated energy E<sub>cum</sub> are the optimal IMs that occur more often among the transition states. Specifically, the E<sub>cum</sub> and the E - ASA<sub>R<sub>67</sub></sub> are directly correlated with acceleration and energy content (see how they are

defined in Table A.1); whilst the I<sub>F</sub> is correlated with velocity terms. Besides, the E - ASA<sub>R<sub>67</sub></sub> is the only one that is repeated on all the transition states. As deeply investigated in [19], this IM is particularly suited to capture the drop and frequency shifts of equipment characterized by a significant spectral acceleration close to the dominant frequency interval of the main structure. These observations agree with the experimental evidence described in [20]. Indeed, the shake table data revealed a significant positive correlation between the maximum floor spectral acceleration  $S_{a,\text{floor}}(T_1)$  and the E - ASA<sub>R<sub>67</sub></sub> for the vertical tank.

Thus, Fig. C.1 reports the state-dependent fragility functions for the industrial component with the optimal IM for each transition state. Dark-red lines and the associated shaded areas highlight the 50%, 90% and 99% confidence bounds, respectively. As the structure reaches the damage level DS<sub>2</sub>, E<sub>cum</sub> is the optimal IM for both pristine and damaged initial level conditions. It can be noted that given a damage limit state to attain, i.e., (graphically) for elements of the same column, the magnitude of IM required to reach the same exceedance probability is lower with the damaged initial conditions. For instance, the 50% probability of exceedance DS<sub>2</sub> given DS<sub>0</sub> and DS<sub>1</sub> is associated to E<sub>cum</sub> = 9 and E<sub>cum</sub> = 3, respectively.

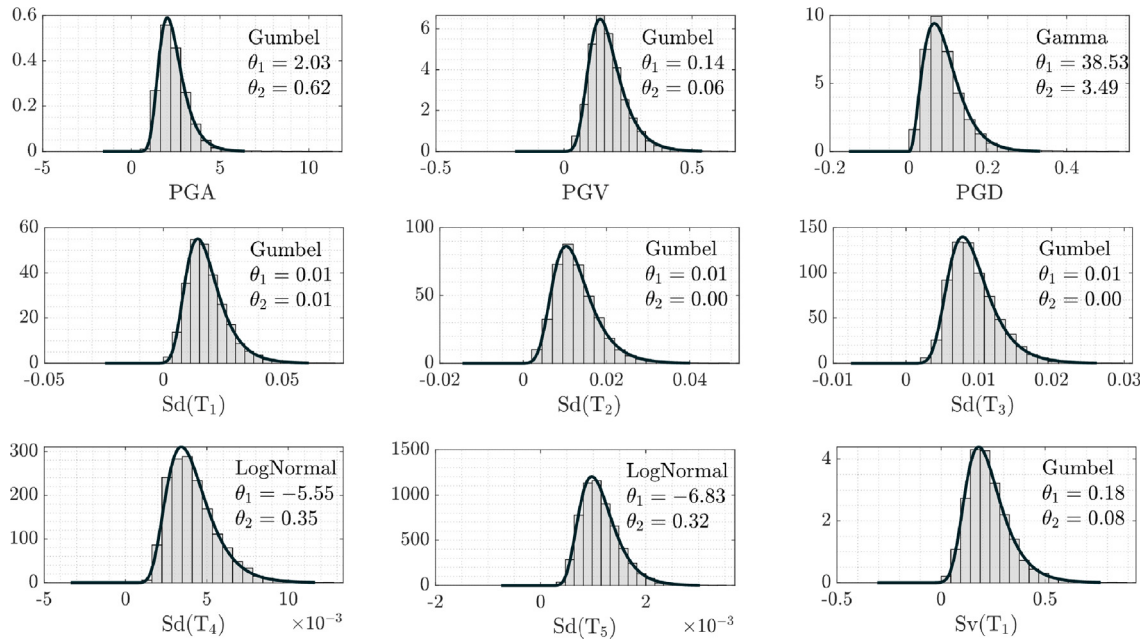


Fig. A.2. Histograms and distributional models for IMs from 1 to 9.

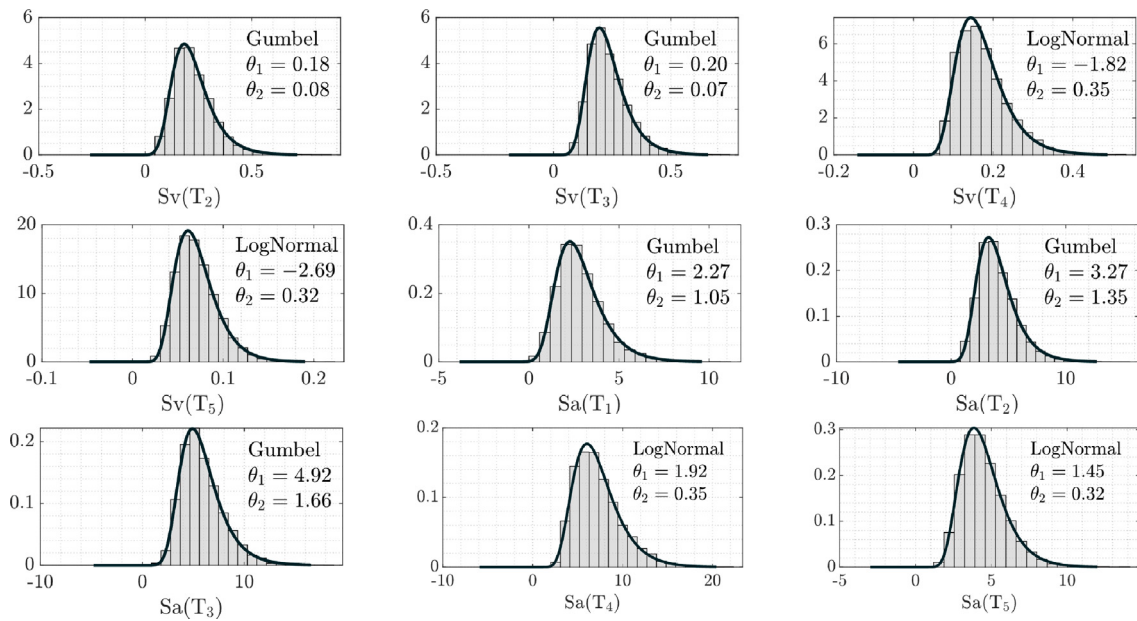


Fig. A.3. Histograms and distributional models for IMs from 10 to 18.

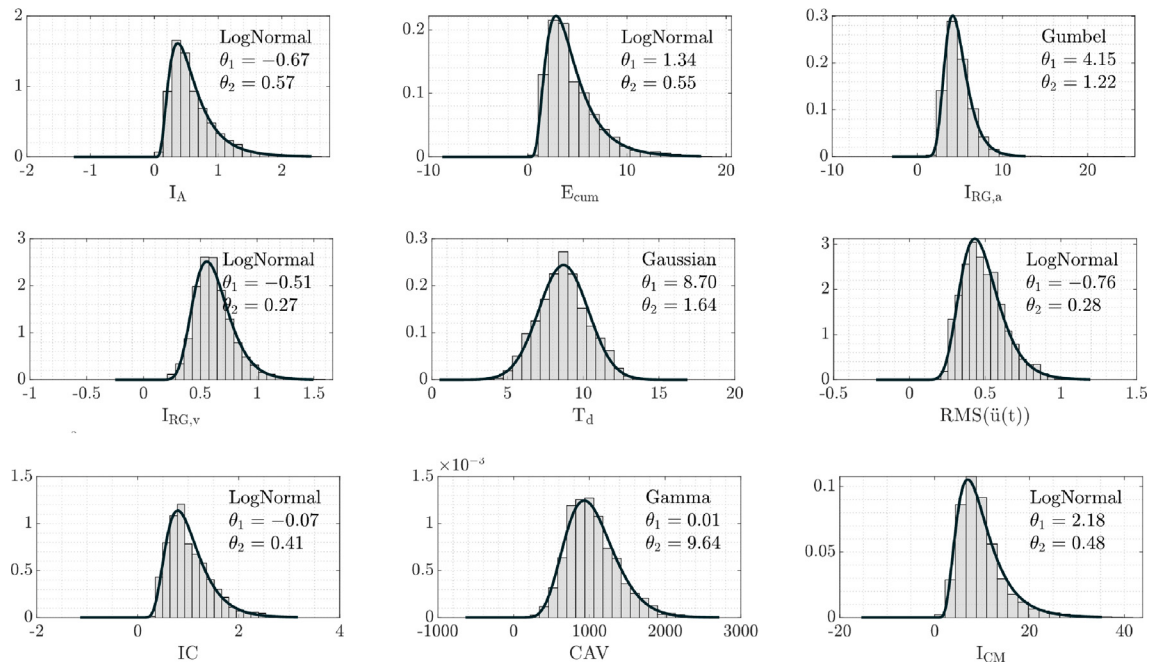


Fig. A.4. Histograms and distributional models for IMs from 19 to 27.

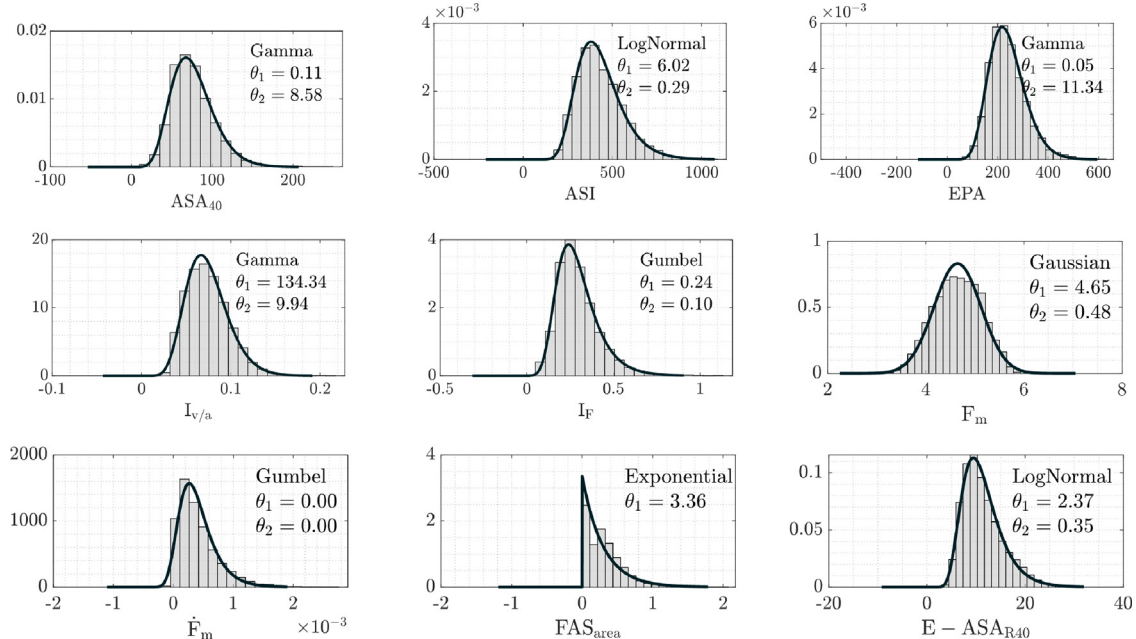


Fig. A.5. Histograms and distributional models for IMs from 28 to 36.

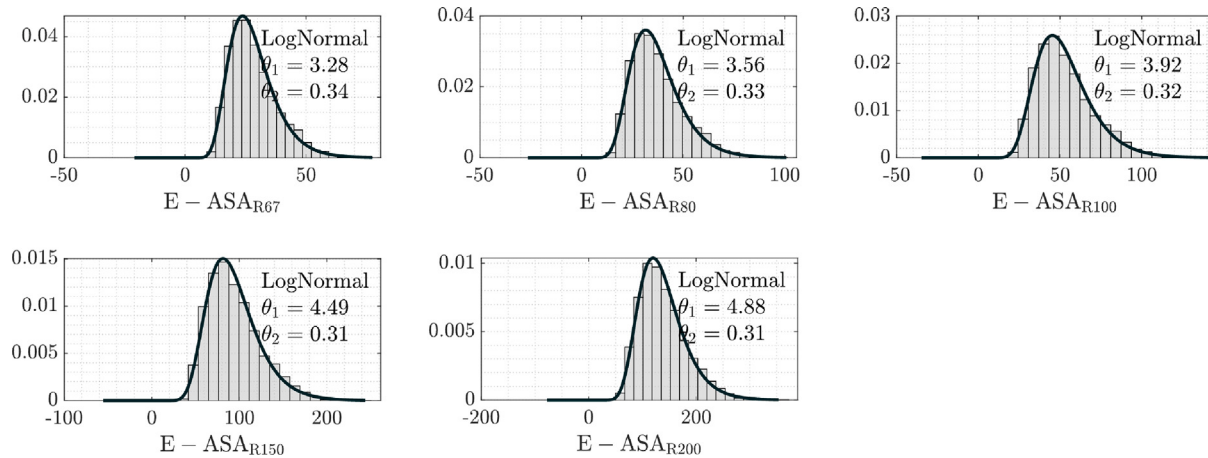


Fig. A.6. Histograms and distributional models for IMs from 37 to 41.

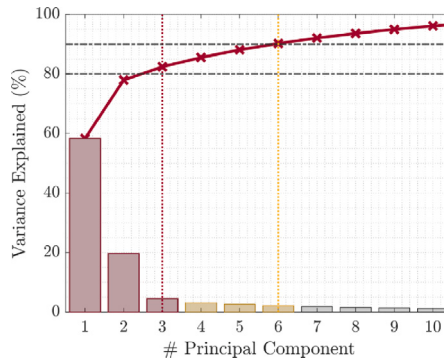


Fig. A.7. Scree plot of the seismic input.

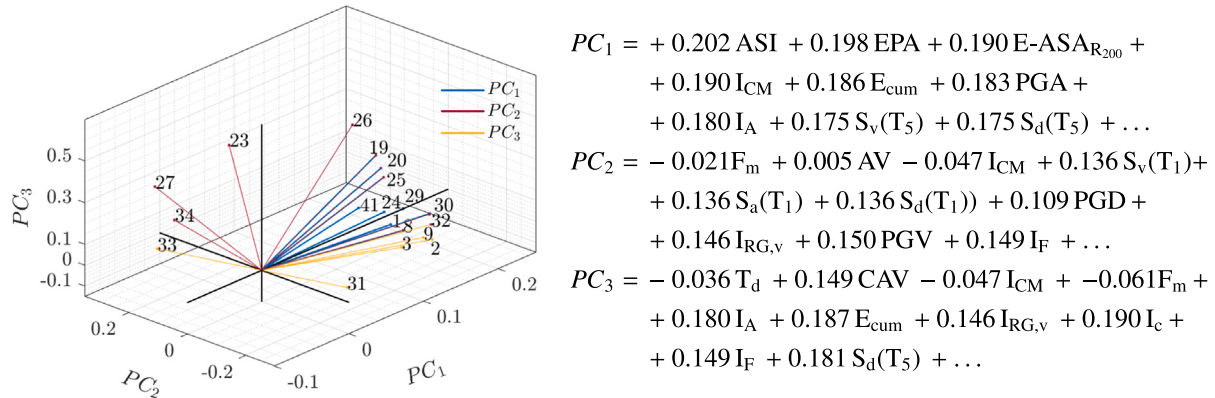
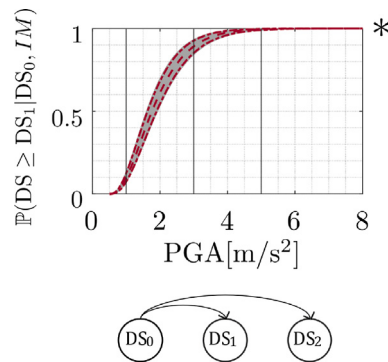
Fig. A.8. 3D biplots of PCs 1, 2 and 3 for the IMs. For clarity, only the relevant  $im_i$ , identified by numbers as labelled in Table A.1, are depicted.

Table C.3

Top five-ranked IM  $\beta_{eff}$  efficiency indices for each transition state.

Frag. '0-0' optimal IM	$\beta_{eff}$ index	Frag. '0-1' optimal IM	$\beta_{eff}$ index	Frag. '0-2' optimal IM	$\beta_{eff}$ index	Frag. '1-1' optimal IM	$\beta_{eff}$ index	Frag. '1-2' optimal IM	$\beta_{eff}$ index
$I_F$	5.00E-04	$I_F$	2.00E-04	$E_{cum}$	1.02E-04	$I_F$	3.00E-04	$E_{cum}$	6.96E-04
PGA	1.24E-02	$E_{cum}$	7.00E-04	$I_A$	9.25E-06	PGA	6.90E-03	$S_v(T_1)$	4.46E-03
$I_C$	3.75E-02	$I_A$	3.80E-03	$I_C$	6.58E-06	$E_{cum}$	4.14E-02	PGA	3.15E-03
$I_{RG,a}$	5.35E-02	$E - ASA_{R67}$	6.70E-03	$I_{CM}$	5.82E-06	$I_{RG,a}$	7.94E-02	$E - ASA_{R67}$	2.58E-03
$E - ASA_{R67}$	8.51E-02	PGA	1.60E-02	$E - ASA_{R67}$	1.81E-06	$E - ASA_{R67}$	9.55E-02	$E - ASA_{R100}$	6.19E-02



**Fig. B.1.** The commonly used "fragility function" evaluated as the exceedance probability, i.e.,  $P(DS \geq DS_1 | DS_0, IM)$ , for PGA as IM.

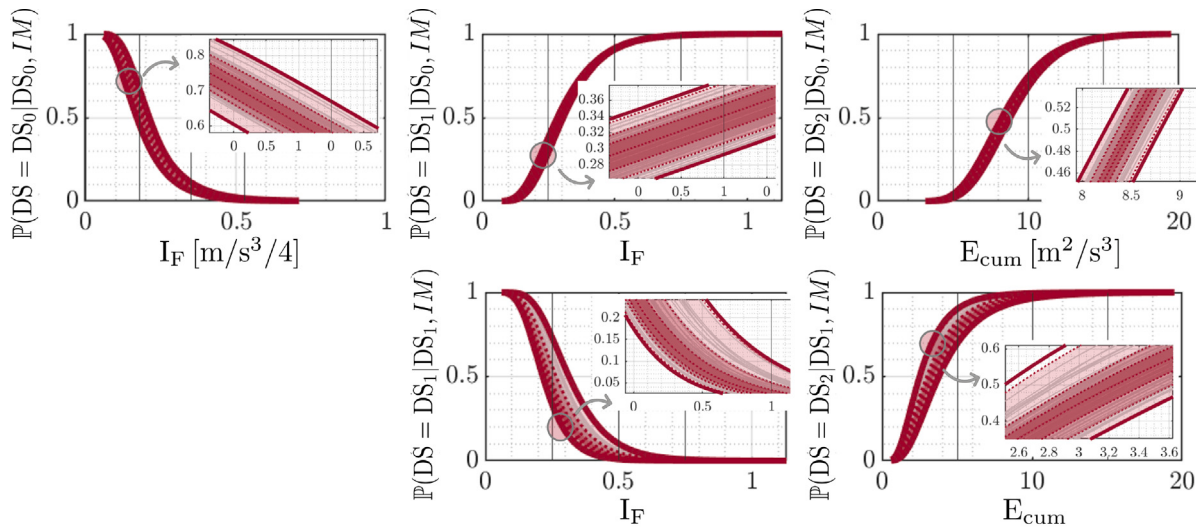


**Fig. C.1.** Bootstrap-PCE state-dependent fragility curves of the SPIF #2 vertical tank: dark-red thick lines stand for the 50%, 90% and 99% confidence bound, along with lighter to darker shaded areas.

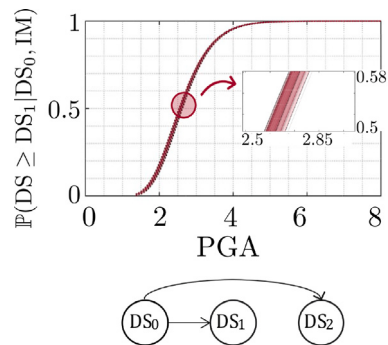


**Fig. C.2.** The commonly used "fragility function" evaluated as the exceedance probability, i.e.,  $P(DS \geq DS_1 | DS_0, IM)$ , with PGA as IM.

## Data availability

Data will be made available on request.

## References

- [1] Du A, Cai J, Li S. Metamodel-based state-dependent fragility modeling for Markovian sequential seismic damage assessment. Eng Struct 2021;243:112644. <http://dx.doi.org/10.1016/j.engstruct.2021.112644>.
- [2] Nguyen M, Lallemand D. Order matters: The benefits of ordinal fragility curves for damage and loss estimation. Risk Anal 2021;42. <http://dx.doi.org/10.1111/risa.13815>.
- [3] Burton HV, Deierlein G, Lallemand D, Lin T. Framework for incorporating probabilistic building performance in the assessment of community seismic resilience. J Struct Eng 2016;142(8):C4015007. [http://dx.doi.org/10.1061/\(ASCE\)ST.1943-541X.0001321](http://dx.doi.org/10.1061/(ASCE)ST.1943-541X.0001321).
- [4] Rincon R, Padgett JE. Fragility modeling practices and their implications on risk and resilience analysis: From the structure to the network scale. Earthq Spectra 2024;40. <http://dx.doi.org/10.1177/87552930231219220>.
- [5] Du A, Padgett JE. Investigation of multivariate seismic surrogate demand modeling for multi-response structural systems. Eng Struct 2020;207:110210. <http://dx.doi.org/10.1016/j.engstruct.2020.110210>.
- [6] Gentile R, Galasso C. Gaussian process regression for seismic fragility assessment of building portfolios. Struct Saf 2020;87. <http://dx.doi.org/10.1016/j.strusafe.2020.101980>.

- [7] Abbiati G, Broccardo M, Abdallah I, Marelli S, Paolacci F. Seismic fragility analysis based on artificial ground motions and surrogate modeling of validated structural simulators. *Earthq Eng Struct Dyn* 2021;50(9):2314–33. <http://dx.doi.org/10.1002/eqe.3448>.
- [8] Iervolino I, Giorgio M, Chioccarelli E. Markovian modeling of seismic damage accumulation. *Earthq Eng Struct Dyn* 2015;45:441–61. <http://dx.doi.org/10.1002/eqe.2668>.
- [9] Di Maio F, Matteo F, Carlo G, Perotti F, Zio E. Time-dependent reliability analysis of the reactor building of a nuclear power plant for accounting of its aging and degradation. *Reliab Eng Syst Saf* 2020;205:107173. <http://dx.doi.org/10.1016/j.ress.2020.107173>.
- [10] Ghosh J, Padgett JE. Aging considerations in the development of time-dependent seismic fragility curves. *J Struct Eng* 2010;136(12):1497–511. [http://dx.doi.org/10.1061/\(ASCE\)ST.1943-541X.0000260](http://dx.doi.org/10.1061/(ASCE)ST.1943-541X.0000260).
- [11] Jia G, Gardoni P. State-dependent stochastic models: A general stochastic framework for modeling deteriorating engineering systems considering multiple deterioration processes and their interactions. *Struct Saf* 2018;72:99–110. <http://dx.doi.org/10.1016/j.strusafe.2018.01.001>.
- [12] Gentile R, Galasso C. Hysteretic energy-based state-dependent fragility for ground-motion sequences. *Earthq Eng Struct Dyn* 2020;50. <http://dx.doi.org/10.1002/eqe.3387>.
- [13] Di Sarno L, Wu J-R. Fragility assessment of existing low-rise steel moment-resisting frames with masonry infills under mainshock-aftershock earthquake sequences. *Bull Earthq Eng* 2021. <http://dx.doi.org/10.1007/s10518-021-01080-6>.
- [14] Pang R, Zai D, Xu B, Liu J, Zhao C, Fan Q, Chen Y. Stochastic dynamic and reliability analysis of AP1000 nuclear power plants via DPIM subjected to mainshock-aftershock sequences. *Reliab Eng Syst Saf* 2023;235:109217. <http://dx.doi.org/10.1016/j.ress.2023.109217>.
- [15] Kassem MM, Nazri FM, Wei LJ, Tan CG, Shahidan S, Zuki SSM. Seismic fragility assessment for moment-resisting concrete frame with setback under repeated earthquakes. *Asian J Civ Eng* 2019;20:465–77. <http://dx.doi.org/10.1007/s42107-019-00119-z>.
- [16] Zhang Y, Burton HV, Sun H, Shokrabiadi M. A machine learning framework for assessing post-earthquake structural safety. *Struct Saf* 2018;72:1–16. <http://dx.doi.org/10.1016/j.strusafe.2017.12.001>.
- [17] Quinci G, Nardin C, Paolacci F, Bursi O. Modelling issues in seismic risk analysis of non-structural components located on industrial plant subsystems. *Bull Earthq Eng* 2023. <http://dx.doi.org/10.1007/s10518-023-01753-4>.
- [18] Filiatroult A, Christopoulos C, Stearns C. Guidelines, specifications and seismic performance characterization of nonstructural building components and equipment. PEER Report 2002/05, Berkeley, CA: University of California; 2001.
- [19] De Biasio M, Grange S, Dufour F, Allain F, Petre-Lazar I. Intensity measures for probabilistic assessment of non-structural components acceleration demand. *Earthq Eng Struct Dyn* 2015. <http://dx.doi.org/10.1002/eqe.2582>.
- [20] Nardin C, Bursi OS, Paolacci F, Pavese A, Quinci G. Experimental performance of a multi-storey braced frame structure with non-structural industrial components subjected to synthetic ground motions. *Earthq Eng Struct Dyn* 2022;51(9):2113–36. <http://dx.doi.org/10.1002/eqe.3656>.
- [21] Mosqueda G, Retamales R, Filiatroult A, Reinhorn A. Testing facility for experimental evaluation of non-structural components under full-scale floor motions. *Struct Des Tall Spec Build* 2009. <http://dx.doi.org/10.1002/tal.441>.
- [22] NIST GCR 17-917-44. Seismic analysis, design, and installation of nonstructural components and systems – background and recommendations for future work. 2017.
- [23] Gardoni P, Der Kiureghian A, Mosalam K. Probabilistic capacity models and fragility estimates for reinforced concrete columns based on experimental observations. *J Eng Mechanics-asce* 2002;128. [http://dx.doi.org/10.1061/\(ASCE\)0733-9399\(2002\)128:10\(1024\)](http://dx.doi.org/10.1061/(ASCE)0733-9399(2002)128:10(1024).
- [24] Gardoni P, Mosalam KM, Der Kiureghian A. Probabilistic seismic demand models and fragility estimates for RC bridges. *J Earthq Eng* 2003;7(sup001):79–106. <http://dx.doi.org/10.1080/13632460309350474>.
- [25] Blatman G. Adaptive sparse polynomial chaos expansions for uncertainty propagation and sensitivity analysis (Ph.D. thesis), Université Blaise Pascal, Clermont-Ferrand; 2009.
- [26] Gidaris I, Taflanidis A, Mavroeidis G. Kriging metamodeling in seismic risk assessment based on stochastic ground motion models: Seismic risk assessment through Kriging metamodeling. *Earthq Eng Struct Dyn* 2015;44. <http://dx.doi.org/10.1002/eqe.2586>.
- [27] Wang J, Sun Z, Cao R. An efficient and robust Kriging-based method for system reliability analysis. *Reliab Eng Syst Saf* 2021;216:107953. <http://dx.doi.org/10.1016/j.ress.2021.107953>.
- [28] Xing L, Gardoni P, Zhou Y, Zhang P. DNN-metamodeling and fragility estimate of high-rise buildings with outrigger systems subject to seismic loads. *Reliab Eng Syst Saf* 2025;253:110572. <http://dx.doi.org/10.1016/j.ress.2024.110572>.
- [29] Zhu X, Broccardo M, Sudret B. Seismic fragility analysis using stochastic polynomial chaos expansions. *Probabilistic Eng Mech* 2023;72:103413. <http://dx.doi.org/10.1016/j.probengmech.2023.103413>.
- [30] Teixeira R, Nogal M, O'Connor A. Adaptive approaches in metamodel-based reliability analysis: A review. *Struct Saf* 2021;89:102019. <http://dx.doi.org/10.1016/j.strusafe.2020.102019>.
- [31] Moustapha M, Marelli S, Sudret B. Active learning for structural reliability: Survey, general framework and benchmark. *Struct Saf* 2022;96:102174. <http://dx.doi.org/10.1016/j.strusafe.2021.102174>.
- [32] Rossetto T, Ioannou I, Grant D. Existing empirical fragility and vulnerability functions: Compendium and guide for selection. *GEM Tech Rep* 2015. <http://dx.doi.org/10.13117/GEM.VULN-MOD.TR2015.012>.
- [33] Ioannou I, Rossetto T, Grant D. Use of regression analysis for the construction of empirical fragility curves. In: Proceedings of the 15th World Conference on Earthquake Engineering (15WCEE). Lisbon, Portugal: International Association for Earthquake Engineering; 2012, [https://www.iitk.ac.in/nicee/wcee/article/WCEE2012\\_2143.pdf](https://www.iitk.ac.in/nicee/wcee/article/WCEE2012_2143.pdf).
- [34] Sudret B. Uncertainty propagation and sensitivity analysis in mechanical models - Contributions to structural reliability and stochastic spectral methods. Clermont-Ferrand, France: Hab. a diriger des recherches, Université Blaise Pascal; 2007.
- [35] Sudret B. Global sensitivity analysis using polynomial chaos expansions. *Reliab Eng Syst Saf* 2008;93(7):964–79. <http://dx.doi.org/10.1016/j.ress.2007.04.002>.
- [36] Federal Emergency Management Agency. Prestandard and commentary for seismic rehabilitation of buildings. FEMA-356 2000.
- [37] Haukaas T, Der Kiureghian A. Finite element reliability and sensitivity methods for performance-based engineering. *Pac Earthq Eng Cent PEER* 2003.
- [38] Rezaeian S, Der Kiureghian A. Simulation of synthetic ground motions for specified earthquake and site characteristics. *Earthq Eng Struct Dyn* 2010. <http://dx.doi.org/10.1002/eqe.997>.
- [39] Hariri-Ardabili M, Saouma V. Probabilistic seismic demand model and optimal intensity measure for concrete dams. *Struct Saf* 2016;59:67–85. <http://dx.doi.org/10.1016/j.strusafe.2015.12.001>.
- [40] Zentner I, Gündel M, Bonfils N. Fragility analysis methods: Review of existing approaches and application. *Nucl Eng Des* 2017;323. <http://dx.doi.org/10.1016/j.nucengdes.2016.12.021>.
- [41] Marelli S, Sudret B. UQLab: A framework for uncertainty quantification in Matlab. In: Vulnerability, uncertainty, and risk (proc. 2nd int. conf. on vulnerability, risk analysis and management (ICVRAM2014), Liverpool, United kingdom). 2014, p. 2554–63. <http://dx.doi.org/10.1061/9780784413609.257>.
- [42] Marelli S, Lüthen N, Sudret B. UQLab user manual – Polynomial chaos expansions, ech. rep., ETH Zurich, Switzerland: Chair of Risk, Safety and Uncertainty Quantification; 2022, Report UQLab-V2.0-104.
- [43] Marelli S, Sudret B. An active-learning algorithm that combines sparse polynomial chaos expansions and bootstrap for structural reliability analysis. *Struct Saf* 2017;75. <http://dx.doi.org/10.1016/j.strusafe.2018.06.003>.
- [44] Lüthen N, Marelli S, Sudret B. Automatic selection of basis-adaptive sparse polynomial chaos expansions for engineering applications. *Int J Uncertain Quantif* 2021;12. <http://dx.doi.org/10.1615/Int.J.UncertaintyQuantification.2021036153>.
- [45] Blatman G, Sudret B. Adaptive sparse polynomial chaos expansion based on least angle regression. *J Comput Phys* 2011;230(6):2345–67. <http://dx.doi.org/10.1016/j.jcp.2010.12.021>, URL <https://www.sciencedirect.com/science/article/pii/S0021999110006856>.
- [46] Perez-Cruz F. Kullback-Leibler divergence estimation of continuous distributions. 2008, p. 1666–70. <http://dx.doi.org/10.1109/ISIT.2008.4595271>.
- [47] Butenweg C, et al. Seismic performance of multi-component systems in special risk industrial facilities. 2020, Deliverable D10.1, SERA Project, Project. No: 730900, H2020-EU.
- [48] SAP2000-v22. Structural analysis and design. 2022, CSI Computer and Structures, Inc..
- [49] Vathi M, Karamanos S, Kapogiannis I, Spiliopoulos K. Performance criteria for liquid storage tanks and piping systems subjected to seismic loading. *J Press Vessel Technol* 2017;139. <http://dx.doi.org/10.1115/1.4036916>.
- [50] Torre E, Marelli S, Sudret B. UQLab user manual – Statistical inference. Tech. rep., Switzerland: Chair of Risk, Safety and Uncertainty Quantification, ETH Zurich; 2024, Report UQLab-V2.1-114.